Loss of MECP2 leads to telomere dysfunction and neuronal stress

Ohashi M, Lee P, Allen D, Fu K, Vargas B, Cinkornpumin J, Salas C, Park, J, Germanguz I, Chronis K, Kuoy E, Wu T, Lin K, Xiao AZ, Chen L, Tran S, Xiao, G, Lin L, Jin P, Pellegrini M, Plath K@ and Lowry WE@

Department of Molecular Cell and Developmental Biology, UCLA

Department of Biological Chemistry, UCLA

Eli and Edythe Broad Center for Regenerative Medicine, UCLA

Molecular Biology Institute, UCLA

Stem Cell Center and Department of Genetics, Yale University

Department of Human Genetics, Emory University

@ To whom correspondence should be addressed/lead contact

William Lowry and Kathrin Plath

Abstract

To determine the role for mutations of MECP2 in Rett Syndrome, we generated isogenic lines of human iPSCs (hiPSCs), neural progenitor cells (NPCs), and neurons from patient fibroblasts with and without MECP2 expression in an attempt to recapitulate disease phenotypes *in vitro*. Molecular profiling uncovered a reduction of 5hmC, increased expression of subtelomeric genes including TERRA (a long non-coding RNA), and shortening of telomeres in the absence of MECP2 in hiPSCs, NPCs, and Neurons. Neurons made without MECP2 show signs of stress, including induction of gamma-H2aX, p53, and senescence, which are typical molecular responses to telomere shortening. The induction of p53 appeared to affect dendritic branching in Rett neurons, as p53 inhibition restored dendritic complexity. Examination of Rett patient brains uncovered similar molecular phenotypes suggesting that our disease-in-a-dish model yielded insights into human Rett Syndrome patient phenotypes and point towards a role for MECP2 in regulating telomere function.

Introduction

Rett Syndrome is a disease associated with loss of function mutations in the gene MECP2, which was originally identified as encoding a methylated DNA binding protein[1-3]. Patient symptoms include microcephaly, intellectual disability, facial dysmorphia, and seizure activity[4,5]. Studies in murine models recapitulate many of the patient phenotypes and have recently identified a role for MECP2 particularly in inhibitory neurons[6-9]. These studies demonstrated that loss of MECP2 can lead to defects in transcription[10-12], dendritic branching[13], nuclear size[3], and AKT signaling[14].

MECP2 is known to bind methlylated DNA (both 5mC and 5hmC)[1,2,15,16], and the loss of MECP2 was shown to affect 5hmC levels in at least one portion of the murine brain. MECP2 has also been described as a transcription factor with specific targets[10,11,13], and more broadly as either a transcriptional activator[14] or repressor[17-20]. However, despite decades of research on MECP2, it is still unclear how mutations in this protein lead to patient symptoms[3,14,21-23]. To confirm findings made in other models and further study these in a human system, some have turned to modeling Rett Syndrome *in vitro* by taking advantage of Disease in a dish approaches. This involves making hiPSCs from patient somatic cells, or using genome engineering to introduce mutations into WT human pluripotent stem cells. In either case, the pluripotent stem cells created are then differentiated toward the neural lineage, and then comparisons can be made between cells that express MECP2 or lack it.

Some of these studies have even taken advantage of isogenically controlled lines to identify both transcriptional and electrophysiological effects of loss of MECP2 in human in vitro models[14,24]. In the current study, we also sought to mitigate the effect of genetic background and variability of differentiation by taking advantage of several isogenic lines of hiPSCs that either express the WT allele or the mutant allele leading to cells that express or lack MECP2[25]. This allowed for detailed molecular analyses of hiPSCs, NPCs and neurons with and without MECP2 under the same genetic background. In addition, several lines were made and analyzed in each category to avoid variance in differentiation potential amongst isogenic lines. Furthermore, isogenic lines were made from two independent patients with different mutations to highlight only those phenotypes associated with loss of MECP2 expression and not genetic background or variance in hPSC differentiation. Finally, we validated many of these findings using siRNA silencing of MECP2 in WT cells of a distinct genetic background.

In comparing multiple lines of cells, it is clear from our data that loss of MECP2 leads to profound molecular alterations specifically towards the ends of chromosomes due to a decrease of 5-hydroxymethylation, induction of subtelomeric gene expression, and shortening of telomeres. The telomere defects that arise in neurons appear to be related to defects in dendritic branching that are a hallmark of the patient disease. Together, these results define a heretofore unappreciated role for MECP2 in molecular regulation towards the ends of chromosomes.

Results

An isogenic model of Rett Syndrome *in vitro*

To determine how loss of MECP2 expression leads to defects in the nervous system we generated a disease-in-a-dish model using iPSCs. Cognizant of the fact that differentiation from hPSCs is highly variable across individual lines, culture conditions, and time, we developed an isogenic model to study Rett Syndrome *in vitro* to remove the confound of genetic background[25]. Because female patients with Rett Syndrome are usually heterozygous for mutant alleles of *MECP2,* fibroblasts isolated from these patients display a mosaic pattern where roughly half the cells express either the mutant or WT allele. This is shown in Figure 1A, where fibroblasts isolated from two patients with distinct mutant alleles of MECP2 (R982 and R567) showed that roughly half the cells express MECP2 while the other half lacked detectable amounts of this protein. One of these mutant alleles is predicted to lead to a premature stop codon, while the other leads to failed transcriptional termination. Reprogramming to iPSCs using a small set of transcription factors has been shown to happen at the clonal level, such that individual reprogramming events in single fibroblasts generate isolated hiPSC clones[26]. Therefore, reprogramming of mosaic fibroblast cultures from two different patients generated single hiPSC clones that either expressed MECP2 protein or lacked it (Fig 1B) (Method described in a previous study[27]). In addition, our work and that of others has shown that under standard conditions, the inactive X chromosome in human fibroblasts does not reactivate upon reprogramming to the pluripotent state[25,27,28], which is distinct from murine reprogramming[29].

Thus, we were able to create multiple lines of hiPSCs with and without MECP2 from individual patients and thereby control for differences in genetic background (shown in Fig 1B are clones made from patient 982, clones from 567 look similar). The hiPSCs generated from fibroblasts of both patients appeared to be unaffected by the lack of MECP2, expressed all appropriate markers, and successfully generated teratomas upon injection into the testes of immunocompromised mice, consistent with previous hiPSC models for loss of MECP2 (Fig 1-figure supplement 1)[14,30-32]. Lack of MECP2 in patient- derived cells and specificity of antibody was also confirmed by western blot (Fig 1-figure supplement 2A). Importantly, we never observed reactivation of the silenced X chromosome that would have resulted in re-expression of the WT allele of MECP2 in any cultures regardless of differentiation status or passage. This is consistent with previous data showing that despite evidence for erosion of isolated portions of the silenced X chromosome[33], the portion containing the MECP2 locus was not affected by reprogramming or differentiation.

As Rett Syndrome primarily afflicts the nervous system and MECP2 is most highly expressed in neurons, we first generated neural progenitor cells from all of the hiPSCs lines following standard protocols[34]. Across at least two lines per patient with and without MECP2, we measured the rate of neuralization, the morphology of NPCs, and expression of typical marker genes. We were unable to detect consistent differences in these properties between multiple clones of both WT and MECP2- lines derived from

both patients (Fig 1C and 1-figure supplement 2B). Furthermore, the growth rate of NPCs with and without MECP2 was not consistently different in NPCs made from either patient (Fig 1-figure supplement 2C). Next, the NPCs were further differentiated by a non-directed differentiation approach that yields both neurons and glia (growth factor withdrawal[35]) (Fig 1D). Both the neurons and glia made from NPCs adopted typical morphologies regardless of MECP2 expression, and all NPCs from both patients produced neurons and glia at the same rate (Fig 1-figure supplement 2D and figure supplement 2E).

Previous studies have also shown that loss of MECP2 in neurons can lead to a decrease in AKT signaling[14]. A similar pattern was observed here in mutant neurons generated from Rett patient hiPSCs as measured by phosphorylation of AKT and S6, while hiPSCs themselves did not seem to be affected by loss of MECP2 (Fig 1E). Dendritic complexity has been shown extensively to be reliant on MECP2 expression in various models of Rett Syndrome, and we found a statistically significant decrease in complexity in neurons made in the absence of MECP2 by Sholl assay (Fig 1F). In addition, we observed qualitative differences in basic neuronal morphology between WT and mutant neurons, where the neurons lacking MECP2 had shorter, thicker processes, and their soma was not as well defined.

Loss of MECP2 leads to disruption of hydroxymethylation of DNA

159 Because MECP2 is a well-established methylated DNA binding protein particularly for 5-
160 hydroxymethylcytosine (5hmC)[16], we analyzed patterns of this mark across the genome
161 in the presence or absence of MECP2 with Methylation-dependent Immunoprecipitation
162 (MEDIP)[41-44] in hiPSCs. We used a stringent criterion to identify differentially
163 hydroxymethylated regions (DhmRs), whereby the indicated regions had to differ by 0.2
164 per million reads per base pair (Fig 2A). We still observed a large number of
165 differentially hydroxymethylated regions (DhmRs) due to the loss of MECP2 in two
166 clones each from two independent patients (982.15 and 982.17 vs 982.16 and 982.18;
167 567.24 and 567.26 vs 567.25).

168

169 The loss of MECP2 led to many more hypomethylated regions than hypermethylated
170 regions, a strong bias that indicated that MECP2 somehow promotes or stabilizes
171 hydroxymethylation (Fig 2B). This hypomethylation is more clearly identified by plotting
172 the Delta Methylation between the WT and MUT clones from both patients. Both
173 patients showed a dramatic shift towards loss of methylation across both clones (Fig
174 2B). Mapping 5hmC-DhmRs relative to genomic features indicated a de-enrichment
175 away from intergenic regions and enrichment at coding exons (Fig 2C indicated by *).
176 When mapping the 5hmC-DhmRs across chromosomal locations, they were highly
177 enriched towards the ends of chromosomes (Fig 2D). In addition, the effect of loss of
178 MECP2 on 5hmC levels was strong enough to be observed by immunostaining in
179 hiPSCs made from both patients (Fig 2E and F).

180

Loss of MECP2 affects the transcriptome of neurons

It has been suggested that loss of MECP2 only affects gene expression in neurons as opposed to the hPSCs and NPCs from which they were derived[14]. Coupled with the fact that 5hmC levels appear to be disturbed in MECP2 null hiPSCs, we sought to determine whether gene expression was affected in hiPSCs, NPCs or neurons in this patient derived *in vitro* model. We therefore proceeded with RNA seq (>120 million reads per sample) of hiPSC, NPC and interneuron cultures. With such sequencing depth, it was possible to analyze the RNA-seq reads for the known mutations present in the patients from which these lines were made (Fig 3-figure supplement 1). This analysis demonstrated that each line studied expressed strictly either the WT or mutant allele of MECP2, and that XCI status was unchanged even after extensive differentiation to neurons.

To optimize the search for molecular effects of loss of MECP2 in hiPSCs, NPCs or neurons, we generated more defined neuronal cultures by following the newly established 3i (three inhibitor) method to create populations of human interneuron progenitors (Fig 3-figure supplement 1A) and interneurons (Fig 3-figure supplement 1B)[45]. Interneurons are particularly relevant in the study of Rett Syndrome as interneuron-specific deletion of Mecp2 in mice recapitulates many of the disease symptoms[6,8,46,47]. We validated the purity and quality of differentiation at each step by immunostaining for markers typical of particular cell types (SOX2, SOX1 and NESTIN as well as FOXG1 and NKX2.1 for NPCs; and Tuj1, MAP2 and GABA for interneurons)

in both WT and MUT cultures followed by quantification (not shown). We first assessed whether interneurons lacking MECP2 also showed diminished dendritic branching. In fact, in patient-derived interneurons made by 3i, defects in dendritic branching as measured by the number of endpoints were clearly observed (Fig 3A).

First, we quantified the expression level of MECP2 in WT cells across these three stages of development and found that the average RPKM was 3.1 for hiPSCs, 4.3 for NPCs, and 7.75 for interneuron cultures. This is consistent with consensus that MECP2 is enriched in neuronal cells, but also demonstrates that it could potentially be relevant to hiPSC and NPC physiology as well. However, high stringency analyses (FDR <0.05) of the RNA-seq data yielded very few gene expression changes due to loss of MECP2 in hiPSCs or NPCs derived from Rett patients (Fig 3B), consistent with Li et al[14]. On the other hand, interneuron cultures made from patient 982 showed many gene expression changes when comparing two individual WT and MUT clones (Fig 3B). Gene ontology analysis uncovered many neuronal physiology- related pathways were downregulated due to loss of MECP2 in neurons, while genes associated with extracellular remodeling and cell migration appeared to be induced (Fig 3C).

We then mapped the interneuron DEGs according to chromosomal location and found an interesting pattern whereby genes that many of the upregulated genes in the absence of MECP2 were enriched towards the ends of chromosomes (Fig 3D). Moreover, the same pattern emerged in analysis of low stringency DEGs (p value

<0.05) from hiPSCs and NPCs lacking MECP2 (Fig S4C and S4D) for the upregulated genes. We did not observe this pattern for the downregulated genes in hiPSCs, NPCs and neurons. These data suggested that MECP2 could play a role in gene regulation particularly at the ends of chromosomes, and was consistent with the pattern observed for hypomethylation of 5hmC in the absence of MECP2. Finally, there was also a small, but statistically significant overlap of 5hmC-DhMRs with DEGs in hiPSCs suggesting a link between the two (Fig 3E).

We validated a number of the subtelomeric gene expression changes induced by loss of MECP2 by RT-PCR in independent preparations of hiPSCs, NPCs and Neurons (Fig 4A). Many of the subtelomeric genes upregulated are typically not expressed at all in hiPSCs, NPCs or neurons, thus the loss of MECP2 led to an aberrant expression pattern as opposed to a reinforcement or suppression of a typical pattern in these cell types. Furthermore, the subtelomeric genes that were induced in the absence of MECP2 were still typically present at less than 1 RPKM, clouding the potential physiological consequence of the induction of these genes.

To determine whether these effects were specific to the genetic background of the cells used or whether defects in reprogramming to the pluripotent state in the absence of MECP2 affected the downstream gene expression pattern, we silenced MECP2 in WT NPCs and assessed gene expression patterns in this context. Several different siRNA targeting oligos were assayed for their ability to silence MECP2 by RT-PCR, western

247 blot, and immunostaining (Fig 4-figure supplement 1). Silencing of MECP2 in either
248 WT-NPCs derived from other pluripotent stem cells or WT-NPCs derived from 15 week
249 old fetal Medial Ganglionic Eminence (MGE) brain tissue, a source of cortical
250 interneuron progenitors[35], led to strong induction of expression of subtelomeric genes
251 (Fig 4B and C).

252

253 Recently, it was discovered that a long non-coding RNA (lncRNA) is also transcribed
254 from the subtelomeric domain into the telomeric sequence itself[48-52]. This lncRNA is
255 both known to be induced by telomere shortening and to potentially negatively regulate
256 telomere length by competing for telomere priming within telomerase[51-53]. TERRA
257 transcripts are difficult to detect by RNA-seq because they contain mostly telomeric
258 repeat sequences. This also makes it difficult to design PCR primers that are specific to
259 a single TERRA transcript. However, we used established RT-PCR primers[51,52] to show
260 that, similar to many subtelomeric genes, several TERRAs were strongly induced in the
261 absence of MECP2 in isogenic derivatives (hiPSCs, NPCs, interneurons) (Fig 4D). In
262 addition TERRA was induced in WT-NPCs derived from pluripotent stem cells or from
263 tissue (Fig 4D).

264

265 **Loss of TET activity phenocopies loss of MECP2**

266 To assess the possibility that MECP2 regulation of 5hmC levels is linked to the
267 regulation of subtelomeric gene expression, we targeted TET enzymes by siRNA. TET
268 enzymes convert 5-methylcytosine (5mC) to 5-hydroxymethylcytosine (5hmC), and their

deletion or downregulation is known to severely diminish levels of 5hmC[44,54]. According to RNA-seq, the three TET enzymes are expressed similarly in both WT and MUT patient neurons (Average RPKM: TET1, 4.1; TET2, 1.6; TET3, 3.6). RT-PCR demonstrated the ability to silence TET 1, 2, and 3 isoforms using a combination of siRNA oligos in neurons (Fig 4E). Assaying for subtelomeric genes, including TERRA transcripts demonstrated that TET inhibition led to strong increases in not only subtelomeric coding genes, but also TERRA transcripts (Fig 4F), in a similar manner as in loss of MECP2, suggesting a link between 5hmC and subtelomeric gene expression. Together, these data confirm that loss of MECP2 can lead to induction of subtelomeric genes, including TERRA, and that this dysregulation could be due to an effect on 5-hydroxymethylation. Left unclear is how the loss of MECP2 leads to changes in 5hmC levels.

Loss of MECP2 leads to telomeric abnormalities

One of the most established functions for TERRAs is their ability to interfere with telomerase function by acting as a competitive inhibitor for telomere priming[55], leading to shortened telomeres. In addition, others have shown that decreased 5hmC in murine embryonic stem cells can also lead to telomere shortening[56], and, as shown here, loss of MECP2 led to decreased 5hmC in hiPSCs (Fig 2). Therefore, we attempted to determine the physiological consequence of TERRA induction in the absence of MECP2. qPCR for telomere length in fact showed that cells without MECP2 showed shorter telomeres, regardless of their stage of differentiation (Fig 5A) (a complete list of

cell lines used for these analyses is provided in Supplemental Table 1). NPCs with transient siRNA knockdown of MECP2 also showed shorter telomeres, indicating that this effect was not simply due to defects during reprogramming or differential expansion of cell lines (Fig 5A). Quantitative fluorescence in situ hybridization (qFISH) was used to determine telomere length at the single cell level. qFISH demonstrated that NPCs without MECP2 showed significantly shorter telomeres relative to centromeric regions (Fig 5B). To further validate these findings we performed southern blot with a telomere probe on NPCs with and without MECP2 and found telomere shortening in cells lacking MECP2 (Fig 5C). These data point towards telomere erosion in the absence of MECP2.

Telomere dysfunction is known to be present in some cancers, and also in cells driven to senescence due to telomere shortening, but this process has yet to be implicated in Rett Syndrome etiology[57-60]. Telomere dysfunction is characterized by short telomeres, induction of PML, gammaH2aX, and p53[61]. We assayed for evidence of telomere dysfunction by immunostaining for gamma-H2aX (Fig 6A) and PML (Fig 6B) in NPCs. WT NPCs with silencing of MECP2 by siRNA and neurons lacking MECP2 also showed clear induction of these marks (data not shown), consistent with telomere dysfunction induced by the absence of MECP2.

Induction of P53 and senescence pathways in the absence of MECP2

312 It is well established that shortening of telomeres puts significant stress on cells, which
313 can lead to senescence or even apoptosis[55,62-64]. As Rett Syndrome is caused by
314 neuronal defects specifically, we determined how neurons lacking MECP2 respond to
315 telomere shortening at the molecular and physiological level. Cells under stress due to
316 telomere shortening are known to induce p53, which can then activate various response
317 pathways downstream such as DNA repair, senescence, and apoptosis[65]. Interestingly,
318 p53 induction due to telomere shortening was previously shown to cause defects in
319 dendritic branching[64,66], which is also the dominant phenotype in Rett Syndrome.
320 Immunostaining for p53 in neurons with and without MECP2 showed a strong increase
321 in p53 protein in the absence of MECP2 (Fig 6C). p21, a transcriptional target gene of
322 p53, was also induced in MECP2 null neurons at the protein level (Fig 6C). In addition,
323 telomere shortening in NPCs due to overexpression of the Progerin allele, which is
324 associated with accelerated aging also induced p53 expression (Fig 6-figure
325 supplement 1E).

326

327 Because telomere shortening is known to also drive cellular senescence, we looked for
328 signs of defective proliferation *in vitro*. While attempting to make clones of fibroblasts
329 from patients with Rett syndrome, we repeatedly found that clones lacking MECP2 did
330 not expand well after a passage (14 MECP2 null clones were created, none expanded),
331 while clones expressing the WT allele expanded without problem (42 MECP2+ clones
332 were created, and 4 out of 4 all expanded). To determine whether MECP2 null
333 fibroblasts encounter senescence, we performed assays to detect endogenous beta-

334 galactosidase, which is known to be a hallmark of this process[67]. Indeed, MECP2 null
335 fibroblasts showed strong activity in this senescence assay (Fig 6D).

336

337 We did not encounter such difficulties with clonal expansion once hiPSCs or hiPSC-
338 derived NPCs were made from patients, presumably because during reprogramming,
339 telomerase is strongly induced to restore telomere length at least beyond the critical
340 threshold[68-73]. In fact, our RNA-seq data showed that hiPSCs made from patients had
341 very high expression of TERT, and NPCs still expressed moderate levels, while neurons
342 did not express appreciable levels (average RPKM for TERT: hiPSC, 8.8; NPC, 1.6;
343 neuron, 0.006). Importantly, the same endogenous galactosidase activity assay on
344 interneurons showed a dramatic increase in senescence activity in neurons lacking
345 MECP2 (Fig 6E). On the other hand, similar assays on NPCs lacking MECP2 did not
346 show any induction of senescence (data not shown). Together, these data indicate that
347 loss of MECP2 leads to the generation of neurons that show evidence of telomere
348 dysfunction.

349

350 Probing RNA-seq data, we also found that MECP2 null interneuron cultures showed a
351 strong increase in a group of genes that are known to be induced by senescent cells,
352 known as the Senescence Associate Secretory Program (SASP). Fig 6-figure
353 supplement 1A shows that SASP genes were strongly induced in MECP2 mutant
354 neurons, providing further evidence of a senescence phenotype. These senescence
355 phenotypes are also intriguing in light of the transcriptional data suggesting an increase

356 in aging- related genes by gene ontology analysis (Fig 3C). The only previous report
357 linking MECP2 loss to senescence was performed by partial silencing of this protein in
358 mesenchymal stem cells, but the results were consistent with those shown here for
359 patient derived MECP2 null fibroblasts[74].

360

361 To demonstrate whether the induction of senescence and p53 observed here was due
362 to telomere shortening as opposed to other molecular phenotypes due to loss of
363 MECP2, we deliberately shortened telomeres in otherwise wildtype NPCs. We took
364 advantage of the progerin allele of the Lamin-A gene. This truncated allele is similar to
365 what is found in patients suffering from Progeria, a premature aging disorder typified by
366 telomere shortening[75,76]. Induction of the progerin allele by lentiviral infection of cDNA
367 in WT NPCs showed a significant telomere shortening as expected (Fig 6-figure
368 supplement 1B). In addition, induction of the progerin allele caused an increase in
369 expression of the same subtelomeric genes and TERRA transcripts that were induced
370 by the loss of MECP2 (Fig 6-figure supplement 1C and D). This was presumably due to
371 the Telomere Position Effect, whereby telomere shortening is known to lead to induction
372 of subtelomeric gene expression[77,78]. Importantly, progerin expression also led to a
373 strong induction of p53 expression (Fig 6-figure 1E), consistent with what was observed
374 in MECP2 null neurons.

375

376 **Blocking induction of P53 can rescue dendritic branching defects due to loss of**
377 **MECP2**

Previous evidence from a murine model of telomere shortening as a result of loss of telomerase complex (TERT) led to defects in dendritic branching, and this effect was strictly dependent on induction of p53[64]. A more recent study also showed that experimentally aging the neural lineage with telomerase inhibition led to neurons with signs of aging, including reduced dendritic branching[79]. Therefore, we posited that inhibition of P53 in MECP2 null neurons with shortened telomeres could potentially restore appropriate dendritic branching.

To determine whether blocking the action of P53 could improve dendritic branching in MECP2 null interneurons, we took advantage of Pifithrin-α, a potent inhibitor of P53 target gene activation[80]. Treatment of MECP2 null interneurons with Pifithrin-α showed evidence of p53 inhibition as measured by RT-PCR for GADD45[65], a target gene important for DNA repair (Fig 6F). After 24-48 hours of p53 inhibition by Pifithrin-α, MECP2 null interneurons appeared to adopt an improved neuronal morphology typified by increased physical distinction between the soma and neurites, longer, thinner neurites, as well as increased dendritic branching as shown and quantified in Fig 6F. These data provide evidence that neurons with shortened telomeres due to loss of MECP2 respond by inducing P53 activity, which then inhibits the formation of complex neuronal processes. In summary, our in vitro model in human neurons suggests that loss of MECP2 leads to aberrant molecular regulation at the ends of chromosomes, leading to telomere shortening and a resulting induction of cell stress pathways such as p53 and senescence (Fig 6G).

Rett patient brains show evidence of telomeric dysfunction

To determine whether any of the phenotypes discovered in this *in vitro* model of Rett Syndrome have relevance to patients afflicted with the disease, we acquired tissue specimens from Rett patients and aged matched controls. We first quantified the degree of chimerism of female Rett patient neurons due to skewing of X chromosome inactivation to determine the relative ratio of neurons that express MECP2 versus those that did not. One of the Rett patient brains showed roughly 75% of its neurons lacking MECP2, while others appeared to have less than 25% MECP2 null neurons (Fig 7A). Southern blotting of the patient brain with 75% mutant neurons compared to an aged-matched control demonstrated that this Rett brain had shorter telomeres (Fig 7B). We then measured telomere length by PCR from genomic DNA isolated from small specimens of brain tissue from a group of Rett patients, and found that some aged matched Rett patient brains showed small decreases in average telomere length (Fig 7C), though not in every case (data not shown). Because of both the limited availability of Rett patient brains, and the variable chimerism of WT and MUT neurons within these Rett brains, perhaps it is not surprising that we were unable to detect trends across all brains analyzed using a method that cannot distinguish between WT and mutant cells. This chimerism, coupled with the known variability of telomere length across even normal individuals and even across brain regions and cell types precludes an accurate assessment of general telomere length differences in Rett brain until more samples become available for study.

On the other hand, we did find that the TERRA transcript was induced in nearly all Rett patient brains as measured by RT-PCR (Fig 7D), suggesting that all the Rett patients display dysregulation at the ends of their chromosomes. We did identify two Rett patient brains with a high proportion of MECP2 null neurons and subjected these to further investigation for signs of telomere dysfunction *in situ*. In patients 1815 and 5784, MECP2 null neurons showed a strong increase in both P53 and PML levels compared to adjacent neurons that expressed MECP2 (Fig 7E and F). This is consistent with the response to telomere shortening due to loss of MECP2 observed *in vitro*. These data are particularly intriguing in light of data showing that telomere shortening diminishes dendritic branching in various types of neurons and that this process can be dependent on p53 activity[64,66].

Discussion

Taken together, these data demonstrate that loss of MECP2 leads to telomere shortening, which in neurons results in clear signs of stress such as H2aX induction, p53/p21 induction, and initiation of a senescence program, all of which suggest that neurons in Rett Syndrome could be in suboptimal health, leading to neurophysiological defects such as dendritic arborization[13,22]. Many of these phenotypes first observed in the *in vitro* model also appeared to be consistent with what could be observed in Rett patient brains, suggesting disease relevance for these findings.

It is curious that telomere defects have not been reported in previous models of Rett Syndrome. While one paper suggested that RNAi-mediated silencing of MECP2 could affect the telomeres of mesenchymal cells[74], decades of work on Rett Syndrome have not uncovered a role for MECP2 in relation to telomeres in a wide variety of models such as various transgenic mouse line, human patient post-mortem analyses, *in vitro* human models. Our study certainly benefited from analyses of multiple isogenically controlled cells from two patients and from the single cell analyses of patients with both WT and MUT neurons in the same area of the brain. This allowed for high confidence comparisons without having to correct for genetic background, or differences in tissue preparation. In addition, the study of telomeres in MECP2 mutant mice could be hampered by the simple fact that telomeres from inbred mouse strains typically used for these studies are on average much longer than human telomeres. Therefore, it is possible that telomere shortening in murine models does not proceed to such an extent by which one would expect induction of p53 in murine models.

Patients with Rett Syndrome are typically characterized by a normal development at birth and subsequent failure to thrive leading to microcephaly and intellectual disability that develops with age. As a result, Rett Syndrome is thought to be caused by experience-dependent loss of neuronal function, which would correlate with data suggesting that MECP2 regulates activity dependent gene expression[10,13,37]. The microcephaly has been proposed to be a function of decreased nuclear size and

dendritic arborization of affected neurons[13,22]. Could the telomere shortening induced senescence described here underlie patient phenotypes? Several studies have looked at the effects of telomere shortening specifically in the neural lineage and found consistently that shortened telomeres leads to upregulation of p53 and decreased dendritic arborization[64,66,81], a phenotype widely described to afflict MECP2 null neurons *in vitro* and *in vivo* (Fig 1).

These results presented here raise the question of whether telomere defects could be common to the etiologies of other ID syndromes. The phenotypes described here show a striking similarity to those observed in hiPSCs and neural derivatives made from patients with Immunodeficiency, centromeric region instability, facial anomalies syndrome (ICF) Syndrome[82-84]. Two independent studies showed that ICF patient-derived hiPSCs displayed subtelomeric hypomethylation, induction of subtelomeric gene expression, TERRA induction and telomere shortening that was coupled to senescence of somatic derivatives such as fibroblasts. ICF Syndrome only partially overlaps with Rett Syndrome in terms of patient phenotypes, but is caused by mutations in DNMT3B, a *de novo* DNA methyltransferase[85]. These findings together are highly relevant as DNMT3B is a key *de novo* methyl transferase to create methylated DNA (5mC), which is the substrate for Tet oxigenases to create 5-hydroxmethylated DNA (5hmC). Recently, another study showed that deletion of Tet enzymes, which are critical to generate the 5hmC mark, led to shortened telomeres[56,86]. Together, these studies demonstrate that DNA hydroxymethylation is important in the regulation of

telomere length, and our data suggest that MECP2 is potentially an important mediator of this effect.

ATRX-related syndrome shares many phenotypic features with Rett Syndrome (ID, seizures, and microcephaly), and the causative gene, ATRX, is known associate with MECP2 both genetically as well as biochemically[87-92]. In murine models of loss of ATRX, telomere shortening and reduced lifespan are observed[93]. The fact that the causative mutations of ICF, Rett and ATRX syndromes are in genes whose products are thought to interact in the regulation of DNA methylation and all possess telomeric defects suggests that the similarities of patient phenotypes could be the result of neuronal response to telomere shortening. This molecular overlap could even form the basis of novel therapeutic strategies that either reverse telomere shortening or block the response of the cell to telomere defects with agents such as Pifithrin, as shown in Fig 6F.

Considering the phenotypes of ICF derived cells, and those of Tet-deleted cells, it seems reasonable to suggest that telomere deficiency could be related to intellectual disability. In addition, subtelomeric and telomeric dysfunction has been implicated in up to 10% of all intellectual disability syndromes[94-96]. Another ID syndrome, Hoyeraal-Hreidarsson, is caused by mutations in RTEL1 (regulator of telomere elongation helicase 1), a factor that interacts with shelterin complex and is critical for telomere elongation[94]. These patients are characterized by low birth weight, microcephaly and

510 immunological dysfunction. Therefore, mutations that specifically result in telomere
511 shortening lead to disease phenotypes similar to those found in patients with loss of
512 MECP2. As a result, we cannot exclude the possibility that telomere shortening during
513 *in utero* development generates neurons that are less well equipped to deal with post-
514 natal stimulation. Furthermore, our analysis of the single male Rett brain specimen
515 available to us suggested that brains completely lacking MECP2 also had shorter
516 telomeres.

517

518 Another possible interpretation of these data is that instead of a failure to mature, Rett
519 Syndrome neurons instead show aspects of premature aging. The fact that MECP2 null
520 neurons have shorter telomeres (Fig 5), show induction of aging related genes including
521 p53 (Fig 3 and 6), and show senescence (Fig 6) are all consistent with this idea[97]. In
522 addition, the fact that WT-NPCs and neurons transduced with the Progerin allele[98],
523 which is known to cause premature aging, show similar phenotypes as neurons lacking
524 MECP2 is also consistent with this idea. On the other hand, while Rett patients suffer
525 from a post-natal cognitive decline, and long term survivors show phenotypes
526 associated with Parkinson's disease[99], the typical phenotypes presented in young
527 female patients are not consistent with premature aging. Whether the physiological
528 response to loss of MECP2 is truly akin to premature aging or whether patients suffer
529 from the effects telomere dysfunction that is unrelated to aging is worthy of continued
530 investigation.

531

Regardless, it is tempting to speculate that treatments that could relieve telomere dysfunction or abrogate the p53 mediated stress response could potentially ameliorate patient outcomes. Pifithrin-α has already been shown to be an effective treatment to restore neuronal function in murine models of injury or stroke[100-102]. Significant future effort will be devoted to determining both whether telomere dysfunction is a common trigger for ID Syndromes, and whether telomere restoration could potentially help patients.

Acknowledgements

We are grateful to Lorenz Studer for sharing the Progerin-GFP and Nuclear-GFP constructs. Human tissue was obtained from the NIH Neurobiobank at the University of Maryland (Baltimore, MD). AZX and TPW are partially supported by Connecticut Regenerative Medicine Foundation (13-SCB-YALE-12). This work was funded by training grants to MO (NIH-Virology and Gene Therapy, UCLA), PL (CIRM, UCLA), CS (CIRM-Bridges, Cal-State-Northridge), DA (HHURP, UCLA). PJ was supported by grants from NIH (KP was supported by NS051630, NS079625 and MH102690). AZX and TPW were supported by the Connecticut Regenerative Medicine Foundation (13-SCB-YALE-12). WEL was supported by a Rose Hills Scholar award through the Eli and Edythe Broad Center for Regenerative Medicine. WEL and KP were supported by NIH (P015P01GM099134). This research was also supported by the Allen Distinguished Investigator Program, through The Paul G. Allen Frontiers Group.

554 ## Materials and Methods

555 *Generation of isogenic Rett Syndrome iPSCs*

556 Two primary fibroblast lines GM17567 (1461A>G in the gene encoding methyl-CpG
557 binding protein 2 (MECP2)), and GM07982 (frameshift mutation, 705delG, in the gene
558 encoding methyl-CpG binding protein 2 (MECP2)), from patients with Rett Syndrome
559 were obtained from Coriell Cell Repositories. 1 x 10^5 fibroblasts were plated in a gelatin
560 coated well of a 6 well plate in MEF media (DMEM/F12 + 10% FBS). After 8-12 hours,
561 the cells were infected with reprogramming lentivirus that harbors polycystronic human
562 Yamanaka factors (Oct4, Klf4, Sox2, cMyc) in DMEM medium containing 10ug/ml of
563 polybrene and incubated overnight at 37^{o}C in 5% CO2 incubator. The following day, the
564 viral media was aspirated, replaced with MEF media and cultured for 3 additional days.
565 Cells were re-plated on the 5th day onto irradiated MEFs in MEF media. On day 6, the
566 culturing media was changed to human ES media containing DMEM/F12 supplemented
567 with L-glutamine, nonessential amino acids (NEAA), penicillin-streptomycin, knockout
568 serum replacement (Invitrogen), and 10 ng/ml basic FGF. Cells were cultured in hiPSC
569 media until iPSC-like colonies were formed. Reprogrammed colonies were further
570 identified by live immunofluorescence staining with TRA-1-81 (Chemicon) then
571 mechanically isolated. Individual colonies were isolated and maintained for at least 2
572 passages before genotyping analysis. For early passages, the iPSCs were propagated
573 mechanically, whereas collagenase was used for subsequent passaging. hiPSCs were
574 cultured as described previously in accordance with the UCLA ESCRO.

575

576 *Generation of teratomas*

577 Generation of teratoma was previously described[103]. Briefly, a single incision was made
578 in the peritoneal cavity of adult SCID mice and the testis was explanted through the
579 incision site. Approximately 60,000 iPSC in a volume of 50 ml 0.5X Matrigel (BD) were
580 transplanted into the testis using a 27-gauge needle. Four to six weeks after surgery,
581 mice were euthanized and the tumors removed for histology. Surgery was performed
582 following Institutional Approval for Appropriate Care and use of Laboratory animals by
583 the UCLA Institutional Animal Care and Use Committee (Chancellor's Animal Research
584 Committee (ARC)).

585

586 *Differentiation in vitro and analysis*

587 Neural specification with neural rosette derivation, neuroprogenitor (NPC) purification,
588 and further differentiation to neurons and glia were performed as described previously
589 [34,104,105]. Relative neuralization efficiency was analyzed by counting the number of
590 neural rosette containing colonies over total number of iPSC colonies. 6-12 35 mm
591 wells were analyzed over four separate experiments. The proliferation efficiency of
592 NPCs was determined by at days 1, 3, and 5 by the total number of cells present in
593 35mm wells seeded at 200,000 cells on day 0. The cells were detached from the plates
594 using accutase (Millipore) then total number of cells per well analyzed using Z1 Coulter
595 particle counter (Beckman Coulter).

596

For spontaneous terminal neuronal differentiation by growth factor withdrawal, NPC cultures were subjected to growth factor withdrawal (removal of EGF and FGF) and cultured in basic medium (DMEMF12 + N2 + B27) with three quarter exchange of media every three days. Cells were cultured up to 20 weeks. Neural differentiation efficiency was analyzed four weeks after growth factor withdrawal by counting the number of cells positive for neuronal markers (MAP2 and Tuj1) over the total number of cells visualized by DAPI. NPCs were transfected with DCX-GFP reporter one day prior to differentiation using Lipofectamine 2000 (Invitrogen). Sholl analysis of DCX-GFP positive neuronal neuritis were also measured using ImageJ. All data values were presented as mean +/- SEM. Student's t-tests were applied to data with two groups. ANOVA analyses were used for comparisons of data with greater than two groups.

For directed differentiation of interneurons, iPSCs were grown on plates coated with matrigel (Corning) until 80% confluency with mTeSR (Stem Cell Technologies). Cells were then treated with DMEM/F12 (GIBCO) containing NEAA (GIBCO), GlutaMAX (GIBCO), bovine serum albumin (Sigma-Aldrich), ß-mercaptoethanol (Sigma-Aldrich), N2 (GIBCO), B27 (GIBCO), SB431542 (10uM; Cayman Chemical), LDN-193189 (100nM; Cayman Chemical) and XAV939 (2uM; Cayman Chemical) later transitioning to the media containing sonic hedgehog (20ng/mL; R&D) and purmorphamine (1uM; Cayman Chemical) as previously described (Maroof et al., 2013). Cells were further differentiated into interneurons with neurobasal medium (GIBCO) containing N2 (GIBCO), B27 (GIBCO), ascorbic acid (Sigma-Aldrich), GlutaMAX (GIBCO), bovine serum albumin (Sigma-Aldrich), ß-mercaptoethanol (Sigma-Aldrich), neurotrophin-3

(10ng/mL; R&D), brain-derived neurotrophic factor (10ng/mL; R&D), and glial cell-derived neurotrophic factor (10ng/mL; R&D).

Neuronal activation

8 weeks *in vitro* differentiated neuronal culture were subjected depolarizing stimulation with 55mM of KCl in basic media for 0hr, 1hr, 5hr and 7hr then isolated for RNA analysis and coverslips fixed with 4% paraformaldehyde for immunostaining.

Western blot

Cells were lysed on ice with RIPA buffer (Pierce) that contains Halt Protease Inhibitor Cocktail (Thermo Fisher Scientific) and Halt Phosphatase Inhibitor Cocktail (Thermo Fisher Scientific). The total protein concentration was measured using BCA Protein Assay Kit (Thermo Fisher Scientific) following the manufacturer's protocol. The lysates containing the equal amount of total protein were mixed with NuPAGE sample buffer (Invitrogen) with 5% mercaptoethanol and denatured at 95 °C for 10 min. Supernatant was electrophoresed onto NuPAGE 4-12% Bis-Tris Protein Gels (Invitrogen) using MOPS running buffer (Invitrogen). Gels were then electroblotted using semi-dry transfer apparatus onto a membrane. The membrane was blocked with 5% non-fat milk for 1 hr and incubated overnight with primary antibodies at 4°C. The next day the membrane was washed and incubated with HRP-conjugated secondary antibodies for 1 hr at room temperature. The membrane was then incubated with ECL Western Blotting

641 Substrate and developed.

642

643 *Immunofluorescence and image quantification*

644 Cells on coverslips were washed with PBS, fixed in 4% paraformaldehyde for 15 min at
645 room temperature, blocked for 1 hr at room temperature with 10% serum and 0.1%
646 Triton-X-100, then incubated overnight at 4 °C with primary antibodies. Frozen tissue
647 sections were thawed to room temperature, fixed in 4% paraformaldehyde for 15 min at
648 room temperature, permeabilized with 0.2% Triton-X-100 for 15 min at room
649 temperature and blocked with 10% serum at 4 °C overnight, followed by incubation with
650 primary antibodies at 4 °C for 16-24 hr. Following primary antibody incubation, the
651 coverslips were incubated with Alexa Fluor (Invitrogen) or Jackson immunoresearch
652 secondary antibodies at room temperature for 1 hr. Cells were counterstained with
653 DAPI and mounted in Prolong Gold (ThermoFisher). Antibodies used include the
654 following: mouse anti-OCT3/4 (1:100, Santa Cruz Biotechnology Inc.), rabbit anti-SOX2
655 (1:300, Cell Signaling Technology), rabbit anti-Nanog (1:100, Cell Signaling
656 Technology), mouse anti-Tra-1-81 (1:250, Chemicon), mouse anti-NESTIN (1:1000,
657 Neuromics), chicken anti-MAP2 (1:2000, Biolegend), chicken anti-GFAP (1:2000,
658 Abcam), rabbit anti-Tubulin β3 (1:500, Covance), mouse anti-p53 (1:500, Cell
659 Signaling), rabbit anti-p21 (1:250, Santa Cruz), mouse anti-PML (1:100, Santa Cruz),
660 mouse anti-phospho-Histone H2A.X (1:2000, EMD Millipore), rabbit anti-5hmc (1:100,
661 Active Motif), rabbit anti MECP2 (1:1000, Diagenode), rabbit anti Foxg1 (1:1000,
662 Abcam), and mouse anti NKX2.1 (1:300, Novocastra). Secondary antibodies

conjugated with Alexa 488, 568, 594, 647 (1:500, Life Technologies) were used. Imaging was performed on Zeiss Axio Imager A1 or Zeiss LSM780 confocal microscope using a 40X or 63X objective on randomly selected cells. Mean intensity or a number of foci were quantified using ImageJ (http://rsb.info.nih.gov/ij/). At least 100 cells per condition were used for each independent experiment.

RT-qPCR

RNA from cultured cells was collected using the RNeasy Mini Kit from Qiagen according to the manufacturer's instructions. The concentration and purity of RNA were measured using nanodrop spectrophotometers (Thermo Scientific). RNA with an A260/A280 ratio in between 1.8 and 2.0 as well as an A260/A230 ratio in between 2.0 and 2.2 was used. RNA was then reverse transcribed using the Super Script III First-Strand cDNA Synthesis kit with Random Hexamers (Invitrogen) according to the manufacturer's instructions. Quantitative PCR was performed using SYBR Green master mix (Roche). Primers were used at a final concentration of 1 uM. Reactions were performed in duplicate and duplicate CT values were averaged and then used for standard $\Delta\Delta$CT analysis. Expression levels were normalized to beta actin. See Supplementary Table 2 for qPCR primer sequences.

Data collection and statistical analysis

683 All the experimental data (RT-qPCR, qPCR assay for telomere length, immunostaining,
684 ß-Galactosidase Senescence Assay) were presented as mean +/- SEM based on at
685 least three biological replicates from independent experiments using the cell lines
686 indicated in Supplementary Table 1. Student's t tests were applied to data with two
687 groups. ANOVA analyses were used for comparisons of data with greater than two
688 groups. A p value < 0.05 was considered as statistically significant.

689

690 *siRNA gene silencing*

691 All knockdown experiments were performed using trilencer siRNAs (from OriGene
692 Technologies) and RNAimax (ThermoFisher) in Opti-MEM media (ThermoFisher).
693 Trilencers were used at a concentration of 20 nM. Transfection media was prepared
694 and then 500,000 cells were plated on top of the transfection media in 6-well plates. The
695 medium was changed to normal NPC media the next day and cells were collected for
696 analysis at the time points indicated.

697

698 *ß-Galactosidase Senescence Assay*

699 ß-Galactosidase Senescence Assay was performed using the Senescence β-
700 Galactosidase Staining Kit from Cell Signaling according to manufacturer's instructions.
701 Briefly, the cells were fixed on coverslips, incubated with X-gal overnight at 37°C, then
702 mounted on glass slides and imaged using a brightfield microscope. The number of
703 blue cells and number of total cells were quantified using the Cell Counter plugin in

704 ImageJ.

705

706 *Quantitative fluorescence in situ hybridization*

707 Cells were fixed with 4% paraformaldehyde for 15 min at RT and permeabilized with
708 0.5% Triton X for 10 min at RT. After dehydration series of 80, 95, and 100% cold
709 ethanol, cells were then treated with RNase (100ug/mL in 2xSSC) for 30 min at 37°C.
710 After washing and another dehydration series, cells were denatured at 85°C for 15 min
711 in the hybridization mix (70% DI formamide, 10 mM Tris-HCl, pH 7.5, 2xSSC, 0.1ug/mL
712 salmon sperm DNA) containing PNA probes (TelC-FITC and Cent-Cy3, Panagene) at
713 1ug/mL and then incubated for 2 hr at RT in dark. After hybridization, cells were washed
714 3X for 5 min in 2xSSC/50% DI formamide, in 2xSSX with 0.1 Tween20, and in 1xSSC.
715 Cells were then counterstained with DAPI and mounted with ProLong Gold
716 (ThermoFisher).

717

718 *Southern blot analysis of terminal restriction fragments (TRF)*

719 Total genomic DNA was extracted using DNeasy Blood and Tissue Kit (Qiagen)
720 following the manufacturer's instruction. Fresh genomic DNA with high purity (an
721 A260/A280 ratio of 1.8) was used for experiments. The integrity of genomic DNA was
722 determined by gel electrophoresis. Southern blotting was carried using a TeloTTAGGG
723 assay kit (Roche Applied Sciences) following the manufacturer's protocol with some
724 modifications (Kimura et al., 2010).

Quantitative PCR assay for average telomere length measurement

Total genomic DNA was extracted using DNeasy Blood and Tissue Kit (Qiagen) following the manufacturer's instruction. The concentration and purity of genomic DNA were measured using nanodrop spectrophotometers (Thermo Scientific). Fresh genomic DNA with high purity (an A260/A280 ratio of 1.8) was used for experiments. The integrity of genomic DNA was determined by gel electrophoresis. QPCR was performed as previously described (Cawthon, 2002) with further modifications (Jodczyk et al., 2015). Briefly, two qPCR reactions were carried using either primers for single copy reference gene (albumin) or telomeres at a final concentration of 900nM (See Supplementary Table 2 for primer sequences). In each reaction, a standard curve was made by serially diluting one reference DNA by 2 fold ranging from 1.56 ng to 50 ng in order to ensure the PCR efficiency of 90-100% with the linear correlation coefficient greater than 0.98 for each independent experiment. 5ng of sample genomic DNA was added in a 384 well plate with a total reaction volume of 15uL. Each reaction was performed in duplicate and duplicate CT values were averaged and then used to calculate for relative telomere copy number to single gene copy number (T/S) ratio.

Quantification of Dendritic Arborization

Neuronal cultures were immunostained for Tuj1 in order to identify mature neurons and visualize entire cells. The stained cells were then imaged at 20x and dendritic arbors of individual cells were traced using the Simple Neurite Tracer plugin for ImageJ. The

number of process ends per cell were counted using the Cell Counter plugin for ImageJ. Only mature neurons—identifiable by their thin processes and condensed somas—were used for analysis. The number of process ends per cell are presented as mean ends per cell +/- SEM. Means were compared using the Student's T-Test for data with two groups. A p value <0.05 was used as the cutoff for significance.

RNA expression profiling

RNA purification was performed with Qiagen RNAeasy kit following the manufacturer's instruction. Libraries were prepared according to the manufacturers guidelines using The TruSeq V2 kit (Illumina). Microarray profiling was performed with Affymetrix Human HG-U133 2.0 Plus arrays as described [106]. For RNA sequencing, the datasets were mapped with RASER and HISAT2. The reads were counted per gene. Genes were defined by the exon union from the hg19 ensembl annotations. The function of DESeq in DESeq2 package was used to first normalize the gene read counts data and then identified the differentially expressed genes. The MA plot was generated with the function of plotMA in DESeq2 package. Q-value of 0.05 is regarded as the stringent cutoff of calling DEGs while p-value less than 0.05 is regarded as the low stringency cutoff. For the meta-chromosome plot of DEGs, all the chromosomes (except chromosome Y) were first divided equally into 20bins with different length, and then the number of DEGs in each bin was counted. GO analysis was performed using DAVID.

Analysis of 5hydroxymethyl-cytosine

769 *5hmC capture (hmC-Seal)*

770 Chemical labeling-based 5hmC enrichment was described previously[107]. In brief, five
771 microgram of genomic DNA was sonicated to 100-500 bp, and then mixed with 100 µl
772 reaction buffer (50 mM HEPES at pH 8.0, 25 mM $MgCl_2$, 250 µM UDP-6-N_3-Glu and
773 2.25 µM wild-type β-glucosyltransferase (β-GT)). Reactions were incubated at 37°C for
774 1 hour, and DNA substrates were purified by Qiagen DNA purification kit. 150 µM
775 dibenzocyclooctyne modified biotin were mixed with β-GT-modified DNA. The labeling
776 reaction was performed at 37°C for 2 hours. The biotin-labeled DNA was then enriched
777 by Strepavidin-coupled Dynabeads (Dynabeads MyOne™ Streptavidin T1, Life
778 Technologies) and purified by Qiagen DNA purification kit. The quantity and quality of
779 purified DNA were analyzed by Qubit 3.0 Fluorometer (Invitrogen) and Agilent 2100
780 BioAnalyzer using DNA high sensitivity analysis kits (Agilent Technologies).

781

782 *MeDIP-seq*

783 Methylated DNA Immunoprecipitation (MeDIP) experiments were performed according
784 to the manufacturer's protocol (Active Motif) and described previously [108]. In brief, five
785 microgram of genomic DNA were sonicated to 100-500 bp, and incubated with 5mC-
786 specific antibody (Active Motif) at 4°C overnight. Enriched methylated DNA will be
787 extensively washed and purified by Qiagen DNA purification kit. The quantity and quality
788 of purified DNA were analyzed by Qubit 3.0 Fluorometer (Invitrogen) and Agilent
789 Bioanalyzer using DNA high sensitivity analysis kits (Agilent Technologies).

790

791 *Library Preparation and High-throughput Sequencing*

Enriched DNA from MeDIP and hME-Seal was subjected to library construction using the NEBNext ChIP-Seq Library Prep Reagent Set for Illumina according the manufacturer's protocol. In brief, 25 ng of input genomic DNA or experimental enriched DNA were utilized for each library construction. 150-300 bp DNA fragments were selected by AMPure XP Beads (Beckman Coulter) after the adapter ligation. An Agilent 2100 BioAnalyzer were used to quantify the amplified DNA, qPCR were applied to accurately quantify the library concentration. 20 pM diluted libraries were used for sequencing. 50-cycle single-end sequencing reactions were performed. Image processing and sequence extraction were done using the standard Illumina Pipeline.

Analysis

Bowtie software was used to map the sequenced reads back to the human genome (hg19) with the parameter of allowing up to two mismatches. Only the uniquely mapped reads were then used to generate the piled-up genome coverage of methylation signals. The methylation signals were further normalized by per million mapped reads for following analysis. The human genome was then segmented into bins of 1kilo-base pairs, which allows for the identification of bins which shows most dramatic methylation signals differences between wild-type and mutant samples. The delta methylation signal of 0.2 per million reads was chosen as the cutoff of calling the Differential Methylation Regions. For the meta-chromosome plot, all the chromosomes (except chromosome Y) were divided equally into 20 bins with different length. We then summarized the total methylation signal within each bin and subtracted the signal between wild-type samples

and mutant samples. The subtracted signal was then plotted as the meta-chromosomal plot of methylation differences.

References

1 Meehan, R. R., Lewis, J. D. & Bird, A. P. Characterization of MeCP2, a vertebrate DNA binding protein with affinity for methylated DNA. *Nucleic Acids Res* **20**, 5085-5092 (1992).

2 Lewis, J. D. *et al.* Purification, sequence, and cellular localization of a novel chromosomal protein that binds to methylated DNA. *Cell* **69**, 905-914 (1992).

3 Chen, R. Z., Akbarian, S., Tudor, M. & Jaenisch, R. Deficiency of methyl-CpG binding protein-2 in CNS neurons results in a Rett-like phenotype in mice. *Nat Genet* **27**, 327-331, doi:10.1038/85906 (2001).

4 Bird, A. The methyl-CpG-binding protein MeCP2 and neurological disease. *Biochem Soc Trans* **36**, 575-583, doi:10.1042/BST0360575 (2008).

5 Chahrour, M. & Zoghbi, H. Y. The story of Rett syndrome: from clinic to neurobiology. *Neuron* **56**, 422-437, doi:10.1016/j.neuron.2007.10.001 (2007).

6 Tomassy, G. S., Morello, N., Calcagno, E. & Giustetto, M. Developmental abnormalities of cortical interneurons precede symptoms onset in a mouse model of Rett syndrome. *Journal of neurochemistry* **131**, 115-127, doi:10.1111/jnc.12803 (2014).

7 Kao, F. C., Su, S. H., Carlson, G. C. & Liao, W. MeCP2-mediated alterations of striatal features accompany psychomotor deficits in a mouse model of Rett syndrome. *Brain Struct Funct* **220**, 419-434, doi:10.1007/s00429-013-0664-x (2015).

8 Goffin, D., Brodkin, E. S., Blendy, J. A., Siegel, S. J. & Zhou, Z. Cellular origins of auditory event-related potential deficits in Rett syndrome. *Nat Neurosci* **17**, 804-806, doi:10.1038/nn.3710 (2014).

9 Kang, S. K., Kim, S. T., Johnston, M. V. & Kadam, S. D. Temporal- and Location-Specific Alterations of the GABA Recycling System in Mecp2 KO Mouse Brains. *J Cent Nerv Syst Dis* **6**, 21-28, doi:10.4137/JCNSD.S14012 (2014).

10 Lee, W. *et al.* MeCP2 regulates activity-dependent transcriptional responses in olfactory sensory neurons. *Hum Mol Genet* **23**, 6366-6374, doi:10.1093/hmg/ddu358 (2014).

11 Chen, W. G. *et al.* Derepression of BDNF transcription involves calcium-dependent phosphorylation of MeCP2. *Science* **302**, 885-889, doi:10.1126/science.1086446 (2003).

12 Tudor, M., Akbarian, S., Chen, R. Z. & Jaenisch, R. Transcriptional profiling of a mouse model for Rett syndrome reveals subtle transcriptional changes in the brain. *Proc Natl Acad Sci U S A* **99**, 15536-15541, doi:10.1073/pnas.242566899 (2002).

13 Zhou, Z. *et al.* Brain-specific phosphorylation of MeCP2 regulates activity-dependent Bdnf transcription, dendritic growth, and spine maturation. *Neuron* **52**, 255-269, doi:10.1016/j.neuron.2006.09.037 (2006).

14 Li, Y. *et al.* Global transcriptional and translational repression in human-embryonic-stem-cell-derived Rett syndrome neurons. *Cell Stem Cell* **13**, 446-458, doi:10.1016/j.stem.2013.09.001 (2013).

15 Yakabe, S. *et al.* MeCP2 knockdown reveals DNA methylation-independent gene repression of target genes in living cells and a bias in the cellular location of target gene products. *Genes Genet Syst* **83**, 199-208 (2008).

16 Mellen, M., Ayata, P., Dewell, S., Kriaucionis, S. & Heintz, N. MeCP2 binds to 5hmC enriched within active genes and accessible chromatin in the nervous system. *Cell* **151**, 1417-1430, doi:10.1016/j.cell.2012.11.022 (2012).

17 Nan, X. *et al.* Transcriptional repression by the methyl-CpG-binding protein MeCP2 involves a histone deacetylase complex. *Nature* **393**, 386-389, doi:10.1038/30764 (1998).

18 Nan, X., Cross, S. & Bird, A. Gene silencing by methyl-CpG-binding proteins. *Novartis Found Symp* **214**, 6-16; discussion 16-21, 46-50 (1998).

19 Cross, S. H., Meehan, R. R., Nan, X. & Bird, A. A component of the transcriptional repressor MeCP1 shares a motif with DNA methyltransferase and HRX proteins. *Nat Genet* **16**, 256-259, doi:10.1038/ng0797-256 (1997).

20 Nan, X., Campoy, F. J. & Bird, A. MeCP2 is a transcriptional repressor with abundant binding sites in genomic chromatin. *Cell* **88**, 471-481 (1997).

21 Marchetto, M. C. *et al.* A model for neural development and treatment of Rett syndrome using human induced pluripotent stem cells. *Cell* **143**, 527-539, doi:S0092-8674(10)01186-4 [pii]

10.1016/j.cell.2010.10.016 (2010).

22 Smrt, R. D. *et al.* Mecp2 deficiency leads to delayed maturation and altered gene expression in hippocampal neurons. *Neurobiol Dis* **27**, 77-89, doi:10.1016/j.nbd.2007.04.005 (2007).

23 Luikenhuis, S., Giacometti, E., Beard, C. F. & Jaenisch, R. Expression of MeCP2 in postmitotic neurons rescues Rett syndrome in mice. *Proc Natl Acad Sci U S A* **101**, 6033-6038, doi:10.1073/pnas.0401626101 (2004).

24 Farra, N. *et al.* Rett syndrome induced pluripotent stem cell-derived neurons reveal novel neurophysiological alterations. *Mol Psychiatry* **17**, 1261-1271, doi:10.1038/mp.2011.180 (2012).

25 Tchieu, J. *et al.* Female human iPS cells retain an inactive X-chromosome. *Cell Stem Cell* **October** (2010).

26 Winkler, T. *et al.* No evidence for clonal selection due to lentiviral integration sites in human induced pluripotent stem cells. *Stem Cells* **28**, 687-694, doi:10.1002/stem.322 (2010).

27 Sahakyan, A. *et al.* Human Naive Pluripotent Stem Cells Model X Chromosome Dampening and X Inactivation. *Cell Stem Cell*, doi:10.1016/j.stem.2016.10.006 (2016).

28 Pasque, V. *et al.* X chromosome reactivation dynamics reveal stages of reprogramming to pluripotency. *Cell* **159**, 1681-1697, doi:10.1016/j.cell.2014.11.040 (2014).

29 Maherali, N. *et al.* Directly reprogrammed fibroblasts show global epigenetic remodeling and widespread tissue contribution. *Cell Stem Cell* **1**, 55-70 (2007).

30 Dajani, R., Koo, S. E., Sullivan, G. J. & Park, I. H. Investigation of Rett syndrome using pluripotent stem cells. *J Cell Biochem* **114**, 2446-2453, doi:10.1002/jcb.24597 (2013).

31 Cheung, A. Y. *et al.* Isolation of MECP2-null Rett Syndrome patient hiPS cells and isogenic controls through X-chromosome inactivation. *Hum Mol Genet* **20**, 2103-2115, doi:10.1093/hmg/ddr093 (2011).

32 Hotta, A. *et al.* Isolation of human iPS cells using EOS lentiviral vectors to select for pluripotency. *Nat Methods* **6**, 370-376 (2009).

33 Mekhoubad, S. *et al.* Erosion of Dosage Compensation Impacts Human iPSC Disease Modeling. *Cell stem cell* **10**, 595-609, doi:10.1016/j.stem.2012.02.014 (2012).

34 Patterson, M. *et al.* Defining the nature of human pluripotent stem cell progeny. *Cell research*, doi:10.1038/cr.2011.133 (2011).

35 Patterson, M. *et al.* Defining the nature of human pluripotent stem cell progeny. *Cell Res* **22**, 178-193, doi:10.1038/cr.2011.133 (2012).

36 Benito, E. & Barco, A. The neuronal activity-driven transcriptome. *Mol Neurobiol* **51**, 1071-1088, doi:10.1007/s12035-014-8772-z (2015).

37 Degano, A. L., Park, M. J., Penati, J., Li, Q. & Ronnett, G. V. MeCP2 is required for activity-dependent refinement of olfactory circuits. *Mol Cell Neurosci* **59**, 63-75, doi:10.1016/j.mcn.2014.01.005 (2014).

38 Cohen, S. *et al.* Genome-wide activity-dependent MeCP2 phosphorylation regulates nervous system development and function. *Neuron* **72**, 72-85, doi:10.1016/j.neuron.2011.08.022 (2011).

39 Singleton, M. K. *et al.* MeCP2 is required for global heterochromatic and nucleolar changes during activity-dependent neuronal maturation. *Neurobiol Dis* **43**, 190-200, doi:10.1016/j.nbd.2011.03.011 (2011).

40 Tao, J. *et al.* Phosphorylation of MeCP2 at Serine 80 regulates its chromatin association and neurological function. *Proc Natl Acad Sci U S A* **106**, 4882-4887, doi:10.1073/pnas.0811648106 (2009).

41 Chapman, V. L., Terranova, R., Moggs, J. G., Kimber, I. & Dearman, R. J. Evaluation of 5-methylcytosine and 5-hydroxymethylcytosine as potential biomarkers for characterisation of chemical allergens. *Toxicology* **340**, 17-26, doi:10.1016/j.tox.2015.12.003 (2016).

42 Zhu, L. *et al.* Genome-Wide Mapping of 5mC and 5hmC Identified Differentially Modified Genomic Regions in Late-Onset Severe Preeclampsia: A Pilot Study. *PLoS One* **10**, e0134119, doi:10.1371/journal.pone.0134119 (2015).

43 Zhao, M. T., Whyte, J. J., Hopkins, G. M., Kirk, M. D. & Prather, R. S. Methylated DNA immunoprecipitation and high-throughput sequencing (MeDIP-seq) using low amounts of genomic DNA. *Cell Reprogram* **16**, 175-184, doi:10.1089/cell.2014.0002 (2014).

44 Jin, S. G., Kadam, S. & Pfeifer, G. P. Examination of the specificity of DNA methylation profiling techniques towards 5-methylcytosine and 5-hydroxymethylcytosine. *Nucleic Acids Res* **38**, e125, doi:10.1093/nar/gkq223 (2010).

45 Maroof, A. M. *et al.* Directed differentiation and functional maturation of cortical interneurons from human embryonic stem cells. *Cell Stem Cell* **12**, 559-572, doi:10.1016/j.stem.2013.04.008 (2013).

46 Krishnan, K. *et al.* MeCP2 regulates the timing of critical period plasticity that shapes functional connectivity in primary visual cortex. *Proc Natl Acad Sci U S A* **112**, E4782-4791, doi:10.1073/pnas.1506499112 (2015).

47 Ito-Ishida, A., Ure, K., Chen, H., Swann, J. W. & Zoghbi, H. Y. Loss of MeCP2 in Parvalbumin-and Somatostatin-Expressing Neurons in Mice Leads to Distinct Rett Syndrome-like Phenotypes. *Neuron* **88**, 651-658, doi:10.1016/j.neuron.2015.10.029 (2015).

48 Lopez de Silanes, I. *et al.* Identification of TERRA locus unveils a telomere protection role through association to nearly all chromosomes. *Nat Commun* **5**, 4723, doi:10.1038/ncomms5723 (2014).

49 Thijssen, P. E. *et al.* Chromatin remodeling of human subtelomeres and TERRA promoters upon cellular senescence: commonalities and differences between chromosomes. *Epigenetics* **8**, 512-521, doi:10.4161/epi.24450 (2013).

50 Deng, Z. *et al.* A role for CTCF and cohesin in subtelomere chromatin organization, TERRA transcription, and telomere end protection. *Embo J* **31**, 4165-4178, doi:10.1038/emboj.2012.266 (2012).

51 Porro, A., Feuerhahn, S., Reichenbach, P. & Lingner, J. Molecular dissection of telomeric repeat-containing RNA biogenesis unveils the presence of distinct and multiple regulatory pathways. *Mol Cell Biol* **30**, 4808-4817, doi:10.1128/MCB.00460-10 (2010).

52 Arnoult, N., Van Beneden, A. & Decottignies, A. Telomere length regulates TERRA levels through increased trimethylation of telomeric H3K9 and HP1alpha. *Nat Struct Mol Biol* **19**, 948-956, doi:10.1038/nsmb.2364 (2012).

53 Azzalin, C. M. & Lingner, J. Telomere functions grounding on TERRA firma. *Trends Cell Biol* **25**, 29-36, doi:10.1016/j.tcb.2014.08.007 (2015).

54 Ito, S. *et al.* Role of Tet proteins in 5mC to 5hmC conversion, ES-cell self-renewal and inner cell mass specification. *Nature* **466**, 1129-1133, doi:nature09303 [pii]

10.1038/nature09303 (2010).

55 Balk, B. *et al.* Telomeric RNA-DNA hybrids affect telomere-length dynamics and senescence. *Nat Struct Mol Biol* **20**, 1199-1205, doi:10.1038/nsmb.2662 (2013).

56 Yang, J. *et al.* Tet Enzymes Regulate Telomere Maintenance and Chromosomal Stability of Mouse ESCs. *Cell Rep* **15**, 1809-1821, doi:10.1016/j.celrep.2016.04.058 (2016).

57 Silvestre, D. C. *et al.* Alternative lengthening of telomeres in human glioma stem cells. *Stem Cells* **29**, 440-451, doi:10.1002/stem.600 (2011).

58 Chen, W., Xiao, B. K., Liu, J. P., Chen, S. M. & Tao, Z. Z. Alternative lengthening of telomeres in hTERT-inhibited laryngeal cancer cells. *Cancer Sci* **101**, 1769-1776, doi:10.1111/j.1349-7006.2010.01611.x (2010).

59 Chen, W. *et al.* Telomerase inhibition alters telomere maintenance mechanisms in laryngeal squamous carcinoma cells. *J Laryngol Otol* **124**, 778-783, doi:10.1017/S0022215109992854 (2010).

60 De Lange, T. Telomere-related genome instability in cancer. *Cold Spring Harb Symp Quant Biol* **70**, 197-204, doi:10.1101/sqb.2005.70.032 (2005).

61 Osterwald, S. *et al.* PML induces compaction, TRF2 depletion and DNA damage signaling at telomeres and promotes their alternative lengthening. *J Cell Sci* **128**, 1887-1900, doi:10.1242/jcs.148296 (2015).

62 Lapasset, L. *et al.* Rejuvenating senescent and centenarian human cells by reprogramming through the pluripotent state. *Genes Dev* **25**, 2248-2253, doi:10.1101/gad.173922.111 (2011).

63 Zeichner, S. L. *et al.* Rapid telomere shortening in children. *Blood* **93**, 2824-2830 (1999).

64 Ferron, S. R. *et al.* Telomere shortening in neural stem cells disrupts neuronal differentiation and neuritogenesis. *J Neurosci* **29**, 14394-14407, doi:10.1523/JNEUROSCI.3836-09.2009 (2009).

65 Vaziri, H. & Benchimol, S. From telomere loss to p53 induction and activation of a DNA-damage pathway at senescence: the telomere loss/DNA damage model of cell aging. *Exp Gerontol* **31**, 295-301 (1996).

66 Zhang, P. *et al.* TRF2 dysfunction elicits DNA damage responses associated with senescence in proliferating neural cells and differentiation of neurons. *J Neurochem* **97**, 567-581, doi:10.1111/j.1471-4159.2006.03779.x (2006).

67 Wang, Z., Wei, D. & Xiao, H. Methods of cellular senescence induction using oxidative stress. *Methods Mol Biol* **1048**, 135-144, doi:10.1007/978-1-62703-556-9_11 (2013).

68 West, M. D. & Vaziri, H. Back to immortality: the restoration of embryonic telomere length during induced pluripotency. *Regenerative medicine* **5**, 485-488, doi:10.2217/rme.10.51 (2010).

69 Mathew, R. *et al.* Robust activation of the human but not mouse telomerase gene during the induction of pluripotency. *FASEB journal : official publication of the Federation of American Societies for Experimental Biology* **24**, 2702-2715, doi:10.1096/fj.09-148973 (2010).

70 Vaziri, H. *et al.* Spontaneous reversal of the developmental aging of normal human cells following transcriptional reprogramming. *Regenerative medicine* **5**, 345-363, doi:10.2217/rme.10.21 (2010).

71 Marion, R. M. & Blasco, M. A. Telomere rejuvenation during nuclear reprogramming. *Curr Opin Genet Dev* **20**, 190-196, doi:10.1016/j.gde.2010.01.005 (2010).

72 Marion, R. M. *et al.* Telomeres acquire embryonic stem cell characteristics in induced pluripotent stem cells. *Cell Stem Cell* **4**, 141-154, doi:10.1016/j.stem.2008.12.010 (2009).

73 Suhr, S. T. *et al.* Telomere dynamics in human cells reprogrammed to pluripotency. *PLoS ONE* **4**, e8124, doi:10.1371/journal.pone.0008124 (2009).

74 Squillaro, T. *et al.* Partial silencing of methyl cytosine protein binding 2 (MECP2) in mesenchymal stem cells induces senescence with an increase in damaged DNA. *FASEB J* **24**, 1593-1603, doi:10.1096/fj.09-143057 (2010).

75 Young, S. G., Meta, M., Yang, S. H. & Fong, L. G. Prelamin A farnesylation and progeroid syndromes. *J Biol Chem* **281**, 39741-39745 (2006).

76 Young, S. G., Fong, L. G. & Michaelis, S. Prelamin A, Zmpste24, misshapen cell nuclei, and progeria--new evidence suggesting that protein farnesylation could be important for disease pathogenesis. *J Lipid Res* **46**, 2531-2558 (2005).

77 Robin, J. D. *et al.* Telomere position effect: regulation of gene expression with progressive telomere shortening over long distances. *Genes Dev* **28**, 2464-2476, doi:10.1101/gad.251041.114 (2014).

78 Baur, J. A., Zou, Y., Shay, J. W. & Wright, W. E. Telomere position effect in human cells. *Science* **292**, 2075-2077, doi:10.1126/science.1062329 (2001).

79 Vera, E., Bosco, N. & Studer, L. Generating Late-Onset Human iPSC-Based Disease Models by Inducing Neuronal Age-Related Phenotypes through Telomerase Manipulation. *Cell Rep* **17**, 1184-1192, doi:10.1016/j.celrep.2016.09.062 (2016).

80 Bassi, L. *et al.* Pifithrin-alpha, an inhibitor of p53, enhances the genetic instability induced by etoposide (VP16) in human lymphoblastoid cells treated in vitro. *Mutat Res* **499**, 163-176 (2002).

81 Batista, L. F. *et al.* Telomere shortening and loss of self-renewal in dyskeratosis congenita induced pluripotent stem cells. *Nature* **474**, 399-402, doi:10.1038/nature10084 (2011).

82 Huang, K. *et al.* Selective demethylation and altered gene expression are associated with ICF syndrome in human-induced pluripotent stem cells and mesenchymal stem cells. *Hum Mol Genet* **23**, 6448-6457, doi:10.1093/hmg/ddu365 (2014).

83 Sagie, S. *et al.* Induced pluripotent stem cells as a model for telomeric abnormalities in ICF type I syndrome. *Hum Mol Genet* **23**, 3629-3640, doi:10.1093/hmg/ddu071 (2014).

84 Yehezkel, S. *et al.* Characterization and rescue of telomeric abnormalities in ICF syndrome type I fibroblasts. *Front Oncol* **3**, 35, doi:10.3389/fonc.2013.00035 (2013).

85 Linhart, H. G. *et al.* Dnmt3b promotes tumorigenesis in vivo by gene-specific de novo methylation and transcriptional silencing. *Genes Dev* **21**, 3110-3122, doi:10.1101/gad.1594007 (2007).

86 Lu, F., Liu, Y., Jiang, L., Yamaguchi, S. & Zhang, Y. Role of Tet proteins in enhancer activity and telomere elongation. *Genes Dev* **28**, 2103-2119, doi:10.1101/gad.248005.114 (2014).

87 Pandey, S., Simmons, G. E., Jr., Malyarchuk, S., Calhoun, T. N. & Pruitt, K. A novel MeCP2 acetylation site regulates interaction with ATRX and HDAC1. *Genes Cancer* **6**, 408-421, doi:10.18632/genesandcancer.84 (2015).

88 Kernohan, K. D., Vernimmen, D., Gloor, G. B. & Berube, N. G. Analysis of neonatal brain lacking ATRX or MeCP2 reveals changes in nucleosome density, CTCF binding and chromatin looping. *Nucleic Acids Res* **42**, 8356-8368, doi:10.1093/nar/gku564 (2014).

89 Baker, S. A. *et al.* An AT-hook domain in MeCP2 determines the clinical course of Rett syndrome and related disorders. *Cell* **152**, 984-996, doi:10.1016/j.cell.2013.01.038 (2013).

90 Kurahashi, H., Ohye, T., Inagaki, H., Kogo, H. & Tsutsumi, M. Mechanism of complex gross chromosomal rearrangements: a commentary on concomitant microduplications of MECP2 and ATRX in male patients with severe mental retardation. *J Hum Genet* **57**, 81-83, doi:10.1038/jhg.2011.143 (2012).

91 Kernohan, K. D. *et al.* ATRX partners with cohesin and MeCP2 and contributes to developmental silencing of imprinted genes in the brain. *Dev Cell* **18**, 191-202, doi:10.1016/j.devcel.2009.12.017 (2010).

92 Nan, X. *et al.* Interaction between chromatin proteins MECP2 and ATRX is disrupted by mutations that cause inherited mental retardation. *Proc Natl Acad Sci U S A* **104**, 2709-2714, doi:10.1073/pnas.0608056104 (2007).

93 Watson, L. A. *et al.* Atrx deficiency induces telomere dysfunction, endocrine defects, and reduced life span. *J Clin Invest* **123**, 2049-2063, doi:10.1172/JCI65634 (2013).

94 Deng, Z. *et al.* Inherited mutations in the helicase RTEL1 cause telomere dysfunction and Hoyeraal-Hreidarsson syndrome. *Proc Natl Acad Sci U S A* **110**, E3408-3416, doi:10.1073/pnas.1300600110 (2013).

95 Moog, U. *et al.* Subtelomeric chromosome aberrations: still a lot to learn. *Clin Genet* **68**, 397-407, doi:10.1111/j.1399-0004.2005.00506.x (2005).

96 De Vries, B. B., Winter, R., Schinzel, A. & van Ravenswaaij-Arts, C. Telomeres: a diagnosis at the end of the chromosomes. *J Med Genet* **40**, 385-398 (2003).

97 Tan, F. C., Hutchison, E. R., Eitan, E. & Mattson, M. P. Are there roles for brain cell senescence in aging and neurodegenerative disorders? *Biogerontology* **15**, 643-660, doi:10.1007/s10522-014-9532-1 (2014).

98 Miller, J. D. *et al.* Human iPSC-based modeling of late-onset disease via progerin-induced aging. *Cell Stem Cell* **13**, 691-705, doi:10.1016/j.stem.2013.11.006 (2013).

99 Zoghbi, H. Y. Rett Syndrome and the Ongoing Legacy of Close Clinical Observation. *Cell* **167**, 293-297, doi:10.1016/j.cell.2016.09.039 (2016).

100 Yang, L. Y. *et al.* Post-traumatic administration of the p53 inactivator pifithrin-alpha oxygen analogue reduces hippocampal neuronal loss and improves cognitive deficits after experimental traumatic brain injury. *Neurobiol Dis* **96**, 216-226, doi:10.1016/j.nbd.2016.08.012 (2016).

101 Zhang, P. *et al.* Regenerative repair of Pifithrin-alpha in cerebral ischemia via VEGF dependent manner. *Sci Rep* **6**, 26295, doi:10.1038/srep26295 (2016).

102 Yang, L. Y. *et al.* Post-trauma administration of the pifithrin-alpha oxygen analog improves histological and functional outcomes after experimental traumatic brain injury. *Exp Neurol* **269**, 56-66, doi:10.1016/j.expneurol.2015.03.015 (2015).

103 Lindgren, A. G. *et al.* Loss of Pten causes tumor initiation following differentiation of murine pluripotent stem cells due to failed repression of Nanog. *PLoS One* **6**, e16478, doi:10.1371/journal.pone.0016478 (2011).

104 Patterson, M. *et al.* let-7 miRNAs Can Act through Notch to Regulate Human Gliogenesis. *Stem cell reports*, doi:10.1016/j.stemcr.2014.08.015 (2014).

105 Karumbayaram, S. *et al.* Directed differentiation of human-induced pluripotent stem cells generates active motor neurons. *Stem Cells* **27**, 806-811 (2009).

106 Lowry, W. E. *et al.* Generation of human induced pluripotent stem cells from dermal fibroblasts. *Proc Natl Acad Sci U S A* **105**, 2883-2888 (2008).

107 Song, C. X. *et al.* Selective chemical labeling reveals the genome-wide distribution of 5-hydroxymethylcytosine. *Nat Biotechnol* **29**, 68-72, doi:nbt.1732 [pii]

10.1038/nbt.1732 (2011).

108 Song, C. X., Yi, C. & He, C. Mapping recently identified nucleotide variants in the genome and transcriptome. *Nature biotechnology* **30**, 1107-1116, doi:10.1038/nbt.2398 (2012).

Figure Legends

Figure 1. Generation of isogenic model of Rett Syndrome *in vitro*

A, Fibroblasts isolated from Rett Syndrome patients (R982 and R567) heterozygous for MECP2 mutations exhibit a mosaic pattern of MECP2 expression due to random XCI. Note that roughly 50% of fibroblasts from each patient express MECP2. **B**, Multiple isogenic hiPSC lines were produced from patient 982 with a typical Yamanaka protocol yielding individual isogenic clones with and without MECP2 expression from the same patient, as judged by NANOG and OCT4 staining. **C**, Specification of 982 patient derived hiPSCs towards neural progenitor cells yielded homogenous cultures of NPCs with and without MECP2. **D**, terminal differentiation of 982 patient derived NPCs towards neurons and glial by growth factor withdrawal yielded normal neural derivatives as measured by immunostaining for MAP2 and GFAP. **E**, MECP2+ and MECP2- hiPSCs and neurons were generated from patient 982 (R982.16 and R982.15) and assayed for activity of the AKT pathway by western blot with antibodies that recognize the active forms of Akt and its downstream target S6. **F**, Sholl assay of dendritic complexity was performed on WT vs MUT neurons derived from patient 982. Increased # of branch points indicates increased dendritic complexity, measured as a function of distance from the cell body. *p value < 0.05 according to student's t test. Bar graphs represent mean +/- SEM.

Figure 2. Hypomethylation of 5-hydroxymethylcytosine in MECP2 null cells

A, The overall delta methylation signal distribution is shown. The cutoff was made based on the difference of 0.2 per million reads per base pair. **B,** Number of differential

5hmC regions (DhmRs) are presented as either gain of 5hmC (hypermethylated) or loss of 5hmC (hypomethylated) in each patient line, comparing MECP+ clones to MECP2- clones. Differential hydroxymethylation pattern between clones from 982 and 567 shows the overall delta-methylation as hypomethylation. **C**, Localization of DhmRs within various genomic features relative to the portion of those features in the genome. The highest concentration of DhmRs was found in coding exons (light green). **D**, Mapping DhmRs across metachromosomes representing the relative location across all chromosomes shows an increase in DhmRs towards the ends of chromosomes. The y-axis represents the differences of normalized methylation signal (piled-up signal per million mapped reads) between wild-type and mutant. **E**, Immunostaining for 5hmC in hiPSC clones from patients 982 and 567 indicated that levels of this DNA methylation mark are considerably lower in MECP2 null hiPSC clones. **F**, 5hmC staining was quantified in hiPSCs derived from both patient 567 and 982. *p value < 0.05 according to student's t test. Bar graphs represent mean +/- SEM.

Figure 3. Loss of MECP2 is associated with differential gene expression particularly in neurons.

A, Immunostaining neurons generated from patient 982 for TuJ1, a neuronal-specific marker. **Right,** quantification of dendritic complexity by counting endpoints shows a significant difference between neurons with and without MECP2 made from patient 982. **B,** Volcano plots of differentially expressed genes (DEGs) in hiPSCs, NPCs and Neurons shows that loss of MECP2 has a profound effect on gene expression in

neurons. **C**, Gene ontological analysis of DEGs increased versus decreased in MECP2 null neurons. **D**, DEGs were mapped to a metachromosome to determine their relative location across chromosomes. In general, upregulated DEGs were enriched towards the ends of chromosomes, while downregulated DEGs showed no clear pattern of location. **E**, DEG and DhmRs are statistically significantly overlapped in hiPSCs. This analysis was performed by randomly select the same number of genes with iPSC FDR DEG from the hg19 genes, then calculating the overlapping with hmC DMRs in a permutation test performed 5,000 times. The permutated number of overlapping genes is shown in the parentheses.

Figure 4. Loss of MECP2 leads to induction of subtelomeric genes including TERRA, a long non-coding RNA

A, RT-PCR for subtelomeric genes in hiPSCs, NPCs and neurons derived from patients. **B**, RT-PCR for subtelomeric genes in WT NPCs with silencing of MECP2 by siRNA. **C**, RT-PCR for subtelomeric genes in WT brain tissue derived NPCs with silencing of MECP2 by siRNA. **D**, RT-PCR with the same samples described in **A**, **B** and **C** for TERRA transcripts. **E**, Silencing of TET expression by siRNA was assessed by RT-PCR. **F**, Knockdown of TET followed by RT-PCR for TERRA transcripts and subtelomeric genes also showed that loss of 5hmC is associated with induction of subtelomeric gene expression. In this figure, all data presented are the resulting relative fold change differences found in at least three biologically independent experiments. In addition, student's t-test was performed across all three or more experiments, and those

with a p-value < 0.05 are indicated with an asterisk. Bar graphs represent mean +/- SEM. The identity of cells used in each replicate experiment are described in Supplemental Table 1.

Figure 5. Loss of MECP2 is associated with telomere shortening

A, Quantitative PCR for telomere length based on a ratio of telomere product versus an autosomal locus (T/S ratio) showed that loss of MECP2 in patients or by siRNA for MECP2 is associated with shorter telomeres in hiPSCs, NPCs and neurons. The data presented are the result of at least three biologically independent experiments, and asterisks indicated p-value < 0.05 according to student's t test. Bar graphs represent mean +/- SEM. A complete sample list across all experiments used is provided in Supplemental Table 1. **B**, As an independent method, quantitative FISH was performed for telomere length as a function of centromere size. **Bottom**, quantification of telomere length in NPCs in two separate experiments from patient 982. **C**, Southern blotting with genomic DNA and a telomere specific probe showed telomere shortening in the absence of MECP2 in hiPSCs and NPCs derived from patient 982.

Figure 6. Physiological consequences to telomere shortening in the absence of MECP2

Immunostaining for H2aX and PML can identify cells with telomere dysfunction. **A,** Immunostaining NPCs in the absence of MECP2 showed a strong increase in H2aX,

which was quantified as a function of SOX2 immunostaining in 567 derived NPCs. **B**, Immunostaining NPCs in the absence of MECP2 showed a strong increase in PML, which was quantified as a function of SOX2 immunostaining in 982 derived NPCs. **C**, Immunostaining for p53 and p21, a target of p53, showed an increase of these stress markers in MECP2 null neurons derived from patient 567. **D**, Cells undergoing senescence show upregulation of endogenous b-galactosidase activity. Clones of fibroblasts lacking MECP2 showed strong b-gal activity, while those of WT fibroblasts did not. **E**, The senescence assay applied to neuronal cultures showed a strong increase in the absence of MECP2. **F**, Treatment of MECP2-null neurons with DMSO or Pifithrin, followed by immunostaining with antibody for TuJ1 shows a change in dendritic branching and morphology following treatment with Pifithrin. Bottom left, RT-PCR for GADD45, a p53 target gene, showed that Pifithrin reduced p53 activity. Bottom right, Quantification of branching phenotype across three independent experiments showed a strong increase in branching as measured by the number of endpoints. **G,** Schematic to depict molecular events known to regulate the ends of chromosomes. Shown on the right is the result of loss of MECP2, which according to immunostaining and senescence activity assays, led to neuronal stress and TIF. In this figure, all data resulted from at least three independent experiments. *p value<0.05 according to student's t test. Bar graphs represent mean +/- SEM.

Figure 7. Rett patient brains show telomere shortening and induction of p53

A, Female Rett patient brains show variable XCI skewing in neurons as judged by immunostaining for MECP2, and quantified as a function of DAPI and MAP2 staining. **B**, Southern blotting of genomic DNA with a telomere specific probe shows the average telomere length in both control (5559) and Rett (1815) brain compared to ladder (right). **C**, qPCR from genomic DNA of aged matched Rett patient brains and control brains. **D**, As measured by RT-PCR, Rett patient brains show an increase in TERRA transcripts compared to aged-match controls. N≥3 independent experiments. Bar graphs represent mean +/- SEM. **E,** Extended characterization of patient 1815 and 5784 showed increased expression of PML specifically in MECP2 null neurons in each of these two patient brains. Yellow inset is a magnification of box showing high magnification of PML staining specifically in MECP2 null neurons. Right panel shows quantification of PML signal in Rett patient brain, comparing the signal in MECP2+ versus MECP2- neurons. **F**, Immunostaining Rett brain for MECP2 and p53 shows higher levels of p53 specifically in MECP2- neurons (quantified on the right).

Figure 1-figure supplement 1. hiPSCs lacking MECP2 are pluripotent

Teratoma assay was performed to establish pluripotency of hiPSCs made from Rett patient fibroblasts. The resulting tumors each showed evidence of differentiation towards all three embryonic germ layers.

Figure 1-figure supplement 2. Similarity of NPCs generated with and without MECP2

A, NPCs were produced from isogenic hiPSCs of Rett patient, and assessed by western blot to validate loss of MECP2 and specificity of antibody. Top panel shows that the antibody only recognizes MECP2. Bottom panel shows that in NPCs from both patients, individual clones either express or lack MECP2. **B**, The ability of hiPSCs to generate NPCs was assayed in Rosette formation assay. Lack of MECP2 did not affect rosette formation across multiple lines from both patients. N=4 independent experiments. *p value < 0.05 according to student's t test (for patient R567) or ANOVA (for patient R982). Bar graphs represent mean +/- SEM. **C**, Growth curves show that loss of MECP2 does not affect proliferation of NPCs made from either patient. **D**, 3 weeks of growth factor withdrawal drives NPCs to differentiate into neurons and glia as measured here by immunostaining for MAP2/Tuj1 or S100/GFAP in patient 567 derived cultures. There was no consistent difference in differentiation potential across lines from either patient. N=2 independent experiments. Bar graphs represent mean +/- SEM. **E**, Patient 982 derived cultures also do not show dramatic differences in the presence of neurons or astrocytes as measured by MAP2 and S100. N=3 independent experiments. Bar graphs represent mean +/- SEM.

Figure 3-figure supplement 1. RNA-seq analysis to determine the relative ration of WT versus MUT transcripts of MECP2 in Rett patient derived lines. Detection of WT and MUT transcripts from each of the lines indicated demonstrated a clear bias towards individual alleles in each patient derived line. This analysis indicates XCI status for each allele, and demonstrates that XCI status is unchanged, even after differentiation to neurons.

Figure 3-figure supplement 2. **A**, Immunofluorescence of interneuron progenitors from WT (**top**) or MECP2null (**bottom**) clones. **B**, Immunofluorescence of interneurons generated from a MECP2null hiPSC clone generated by 3i protocol. **C**, Volcano plots of lower stringency DEGs in hiPSCs and NPCs between MECP2+ versus MECP2- clones (p-value < 0.05). **D,** Mapping of low stringency DEGs in hiPSCs and NPCs across metachromosome to measure enrichment of DEG location.

Figure 4-figure supplement 1. Silencing MECP2 by siRNA

MECP2 was downregulated by RNA interference, quantified by RT-PCR (left), for protein by western blot (middle), and as demonstrated by immunostaining for MECP2 (right). N=3 independent experiments. *p value < 0.05 according to student's t test. Bar graphs represent mean +/- SEM.

Figure 6-figure supplement 1. Transduction of Progerin leads to phenotypes similar to loss of MECP2. **A,** Cells undergoing senescence are known to induce and secrete a group of genes called SASP. RNA-seq data from neurons were mined for SASP genes, and shown are those SASP genes that were differentially expressed between patient derived neurons with and without MECP2. **B,** qPCR for telomere length in WT NPCs showed that Progerin infected cells have on average shorter telomeres. N=3 independent experiments. *p value < 0.05 according to student's t test. Bar graphs represent mean +/- SEM. **C**, RT-PCR from progerin infected NPCs showed an

induction of various subtelomeric genes. N≥3 independent experiments. *p value<0.05 according to student's t test. Bar graphs represent mean +/- SEM. **D**, RT-PCR for TERRA transcripts following progerin transduction. N≥3 independent experiments. *p value < 0.05 according to student's t test. Bar graphs represent mean +/- SEM. **E**, Immunostaining for p53 following progerin expression. Quantification of p53 in infected cells (either Nuclear-GFP or Progerin-GFP) is shown on the right. *p value < 0.05 according to student's t test. Bar graphs represent mean +/- SEM.

Supplemental Table 1.

Provided is a list of all cell types analyzed across the RT-PCR and Telomere qPCR experiments performed in this manuscript.

Supplemental Table 2.

Provided is a list of all the primers used in this study.

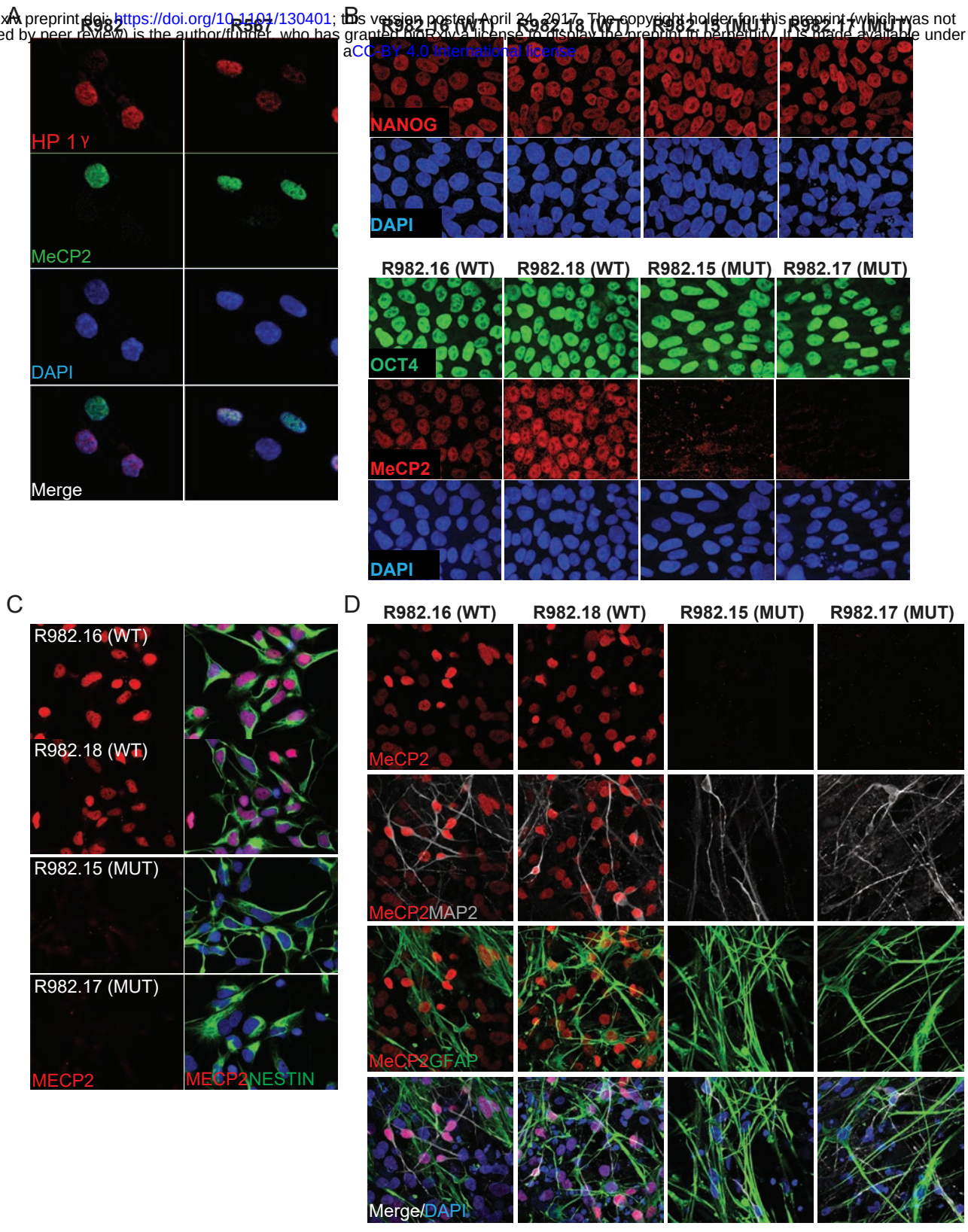

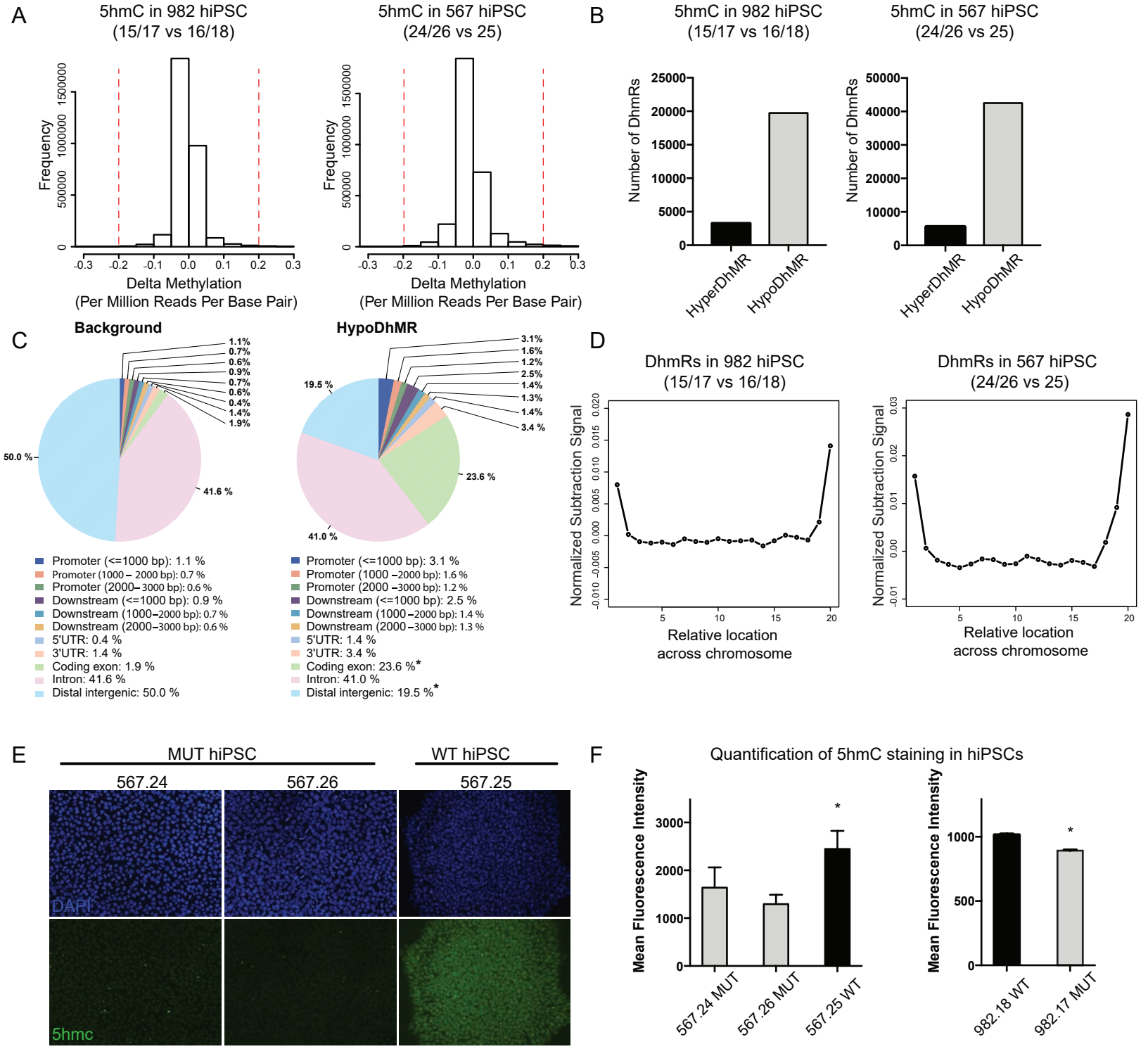

A

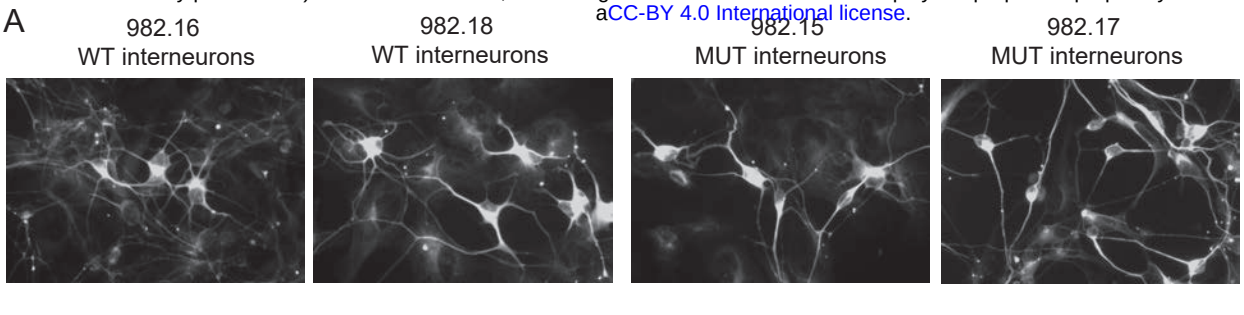

B

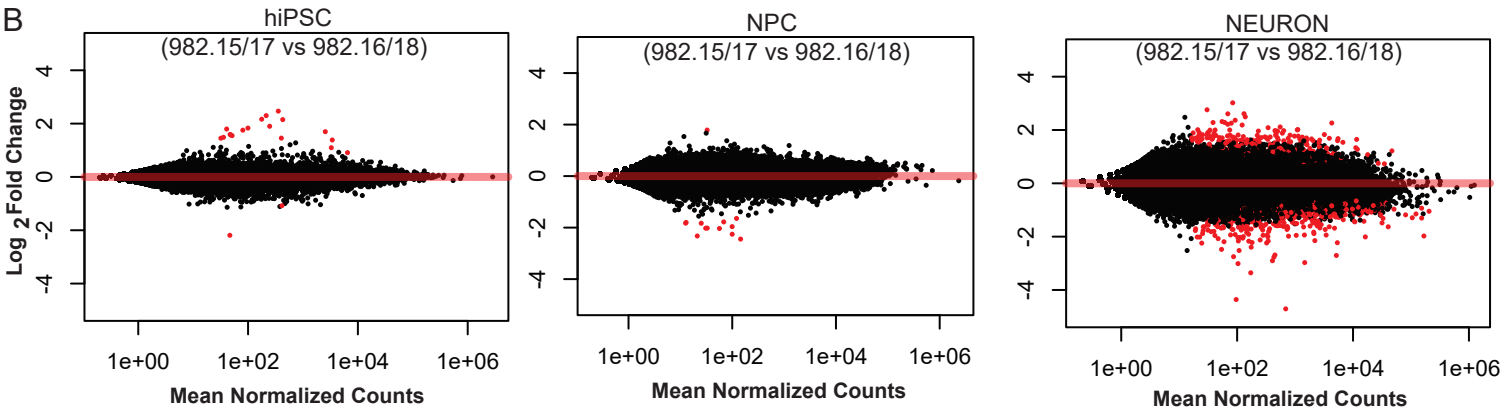

C

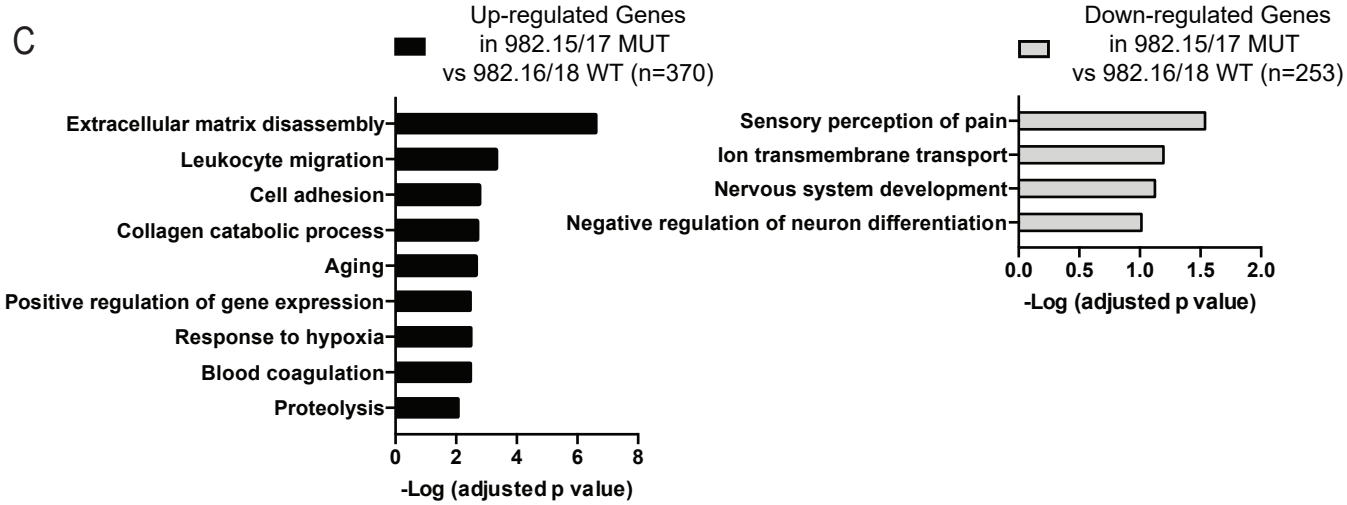

D

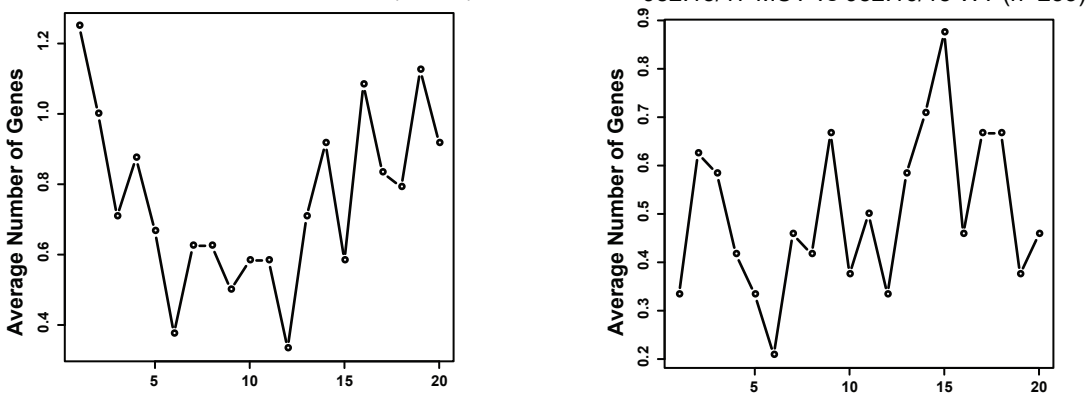

E

Number of DEG (hiPSCs)	Overlap with Hyper DhMR	Overlap with Hypo DhMR
20	5 (1)	19 (6)

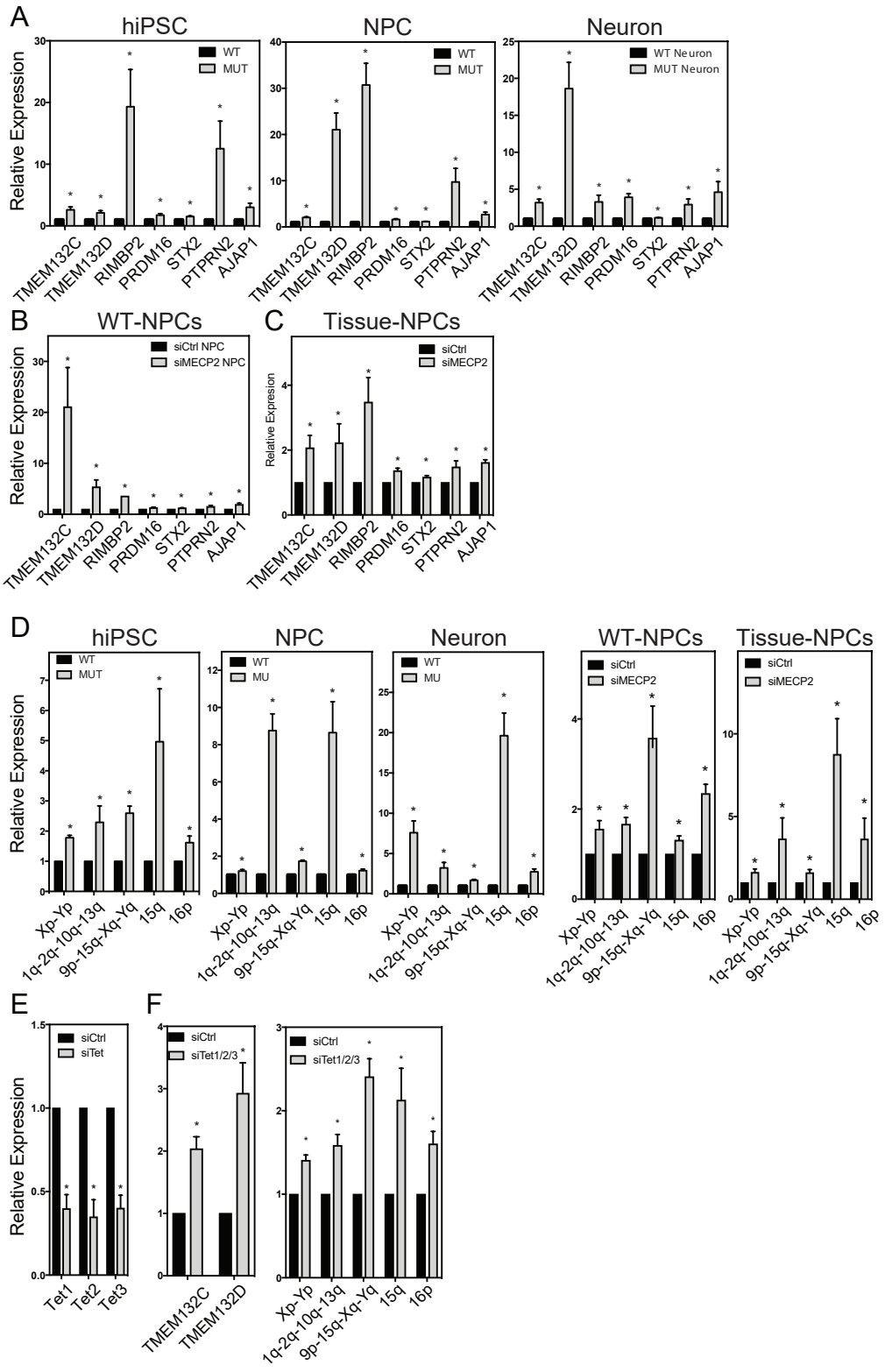

A

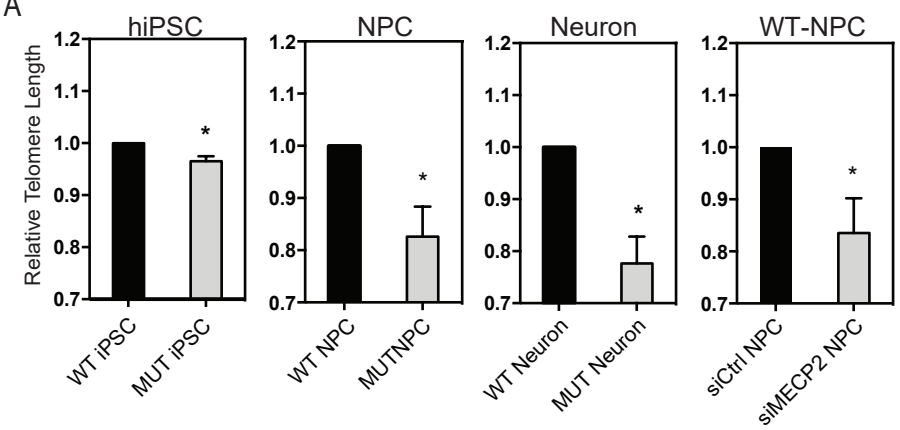

B

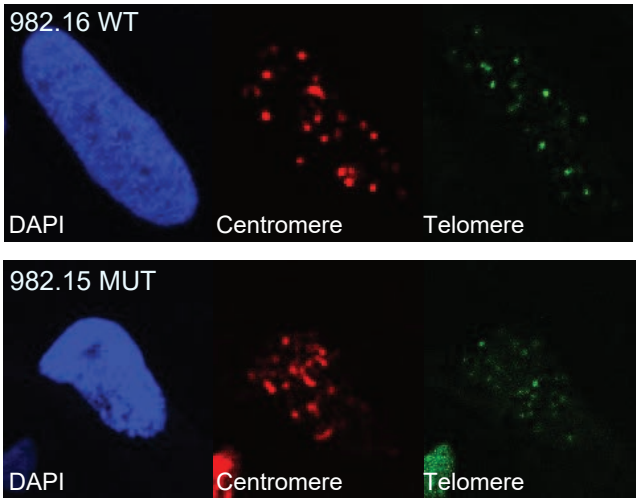

C

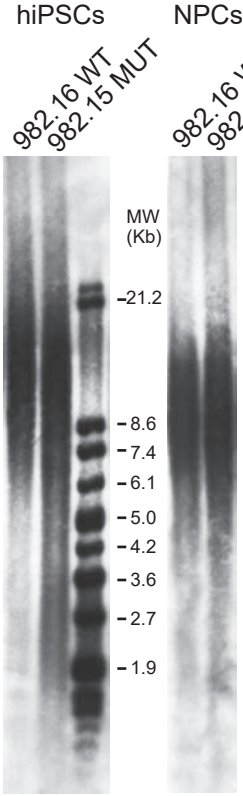

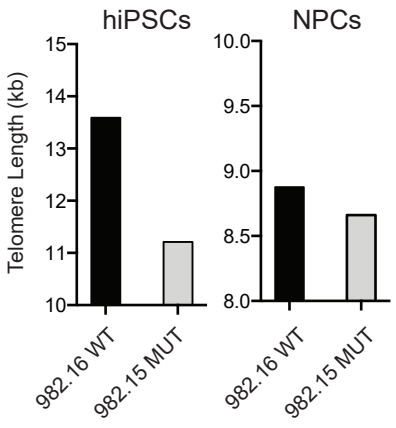

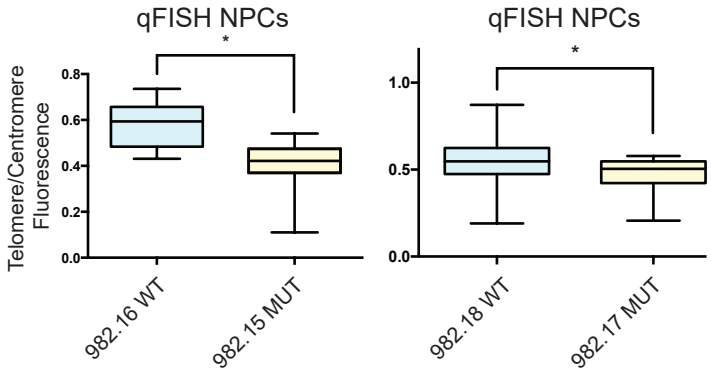

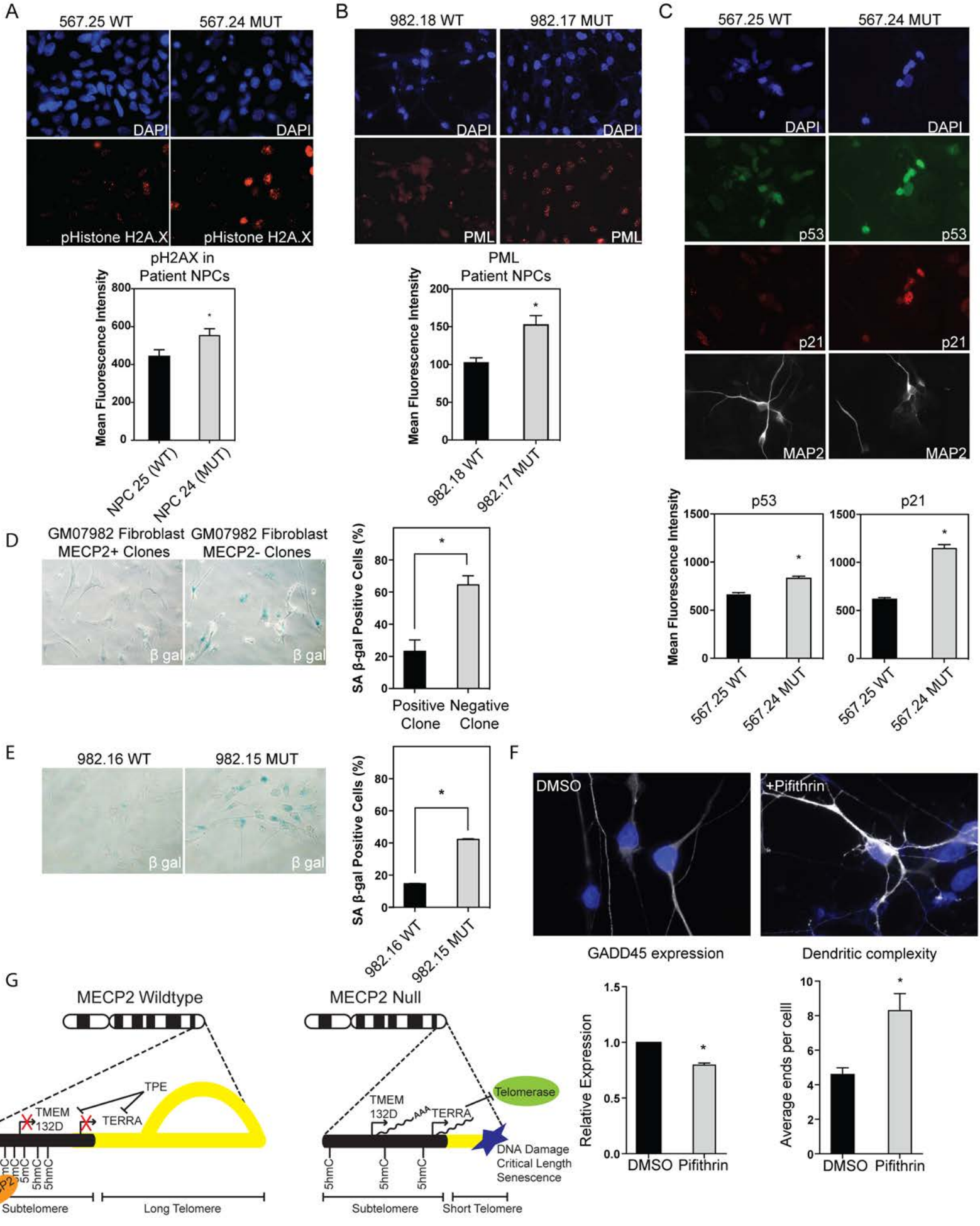

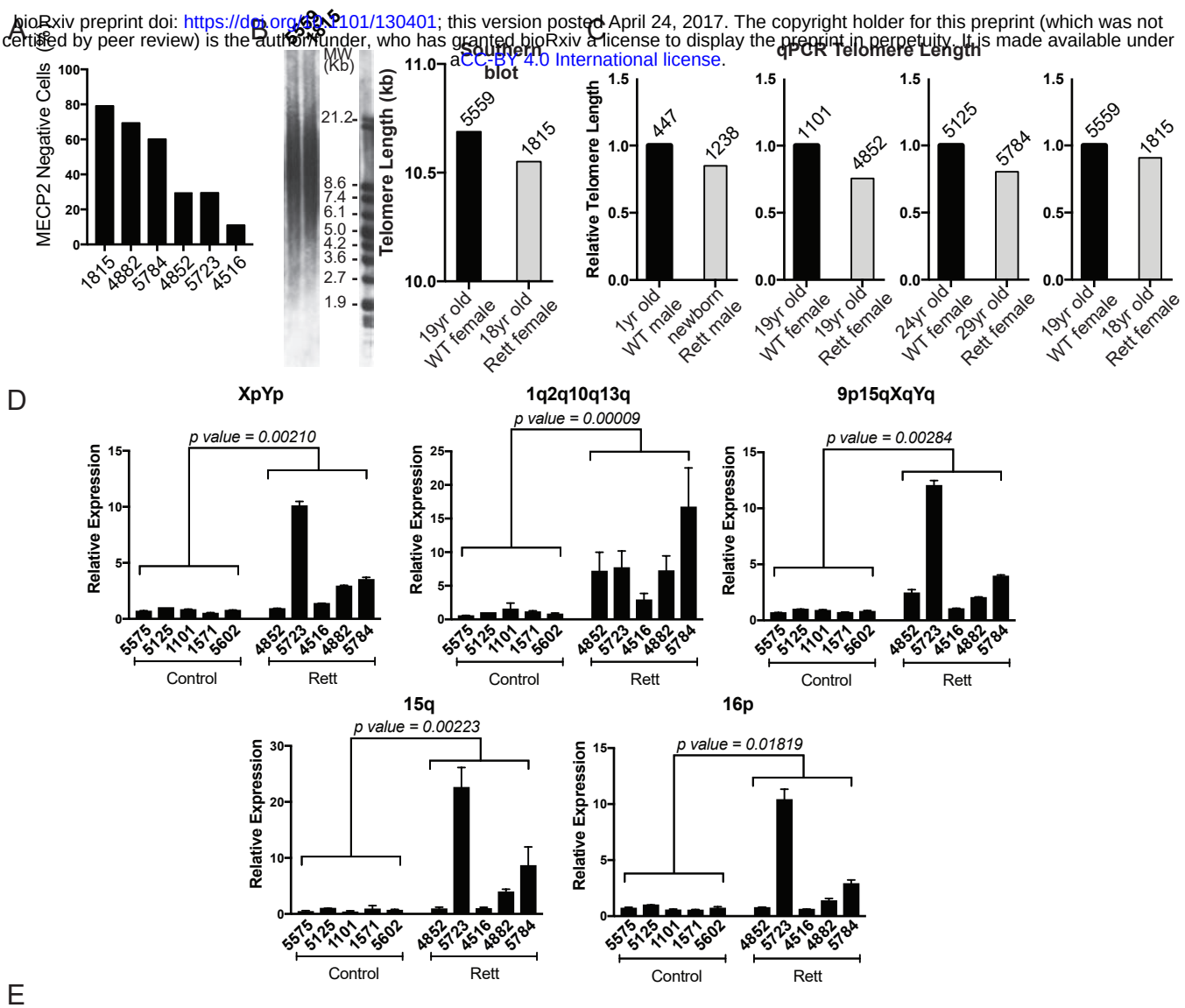

	N (biological	gene	Sample	Correspondir	Date of Experiments
HIPS Terra	3	Xp-Yp	24/25	Fig4D	20151028
			25/26	Fig4D	20151028
			25/26	Fig4D	20151028
	5	1q_2q_10q_1	15/16	Fig4D	20160602
			15/16	Fig4D	20160222
			24/25	Fig4D	20151028
			25/26	Fig4D	20151028
			15/16	Fig4D	20151102
	3	9p_15q_Xq_Y	15/16	Fig4D	20160602
			15/16	Fig4D	20160222
			24/25	Fig4D	20151028
	6	15q	15/16	Fig4D	20160420
			15/16	Fig4D	20160512
			15/16	Fig4D	20151102
			17/18	Fig4D	20160420
			24/25	Fig4D	20151102
			15/16	Fig4D	20160602
	3	16p	17/18	Fig4D	20160420
			15/16	Fig4D	20160222
			24/25	Fig4D	20151102
NPC Terra	4	Xp-Yp	17/18	Fig4D	20151113
			17/18	Fig4D	20151113
			17/18	Fig4D	20151113
			17/18	Fig4D	20151027
	3	1q_2q_10q_1	17/18	Fig4D	20151027
			17/18	Fig4D	20151027
			17/18	Fig4D	20151109
	3	9p_15q_Xq_Y	17/18	Fig4D	20151027
			17/18	Fig4D	20151027
			17/18	Fig4D	20151109
	3	15q	15/16	Fig4D	20150501
			15/16	Fig4D	20151113
			17/18	Fig4D	20151113
	3	16p	17/18	Fig4D	20150508
			17/18	Fig4D	20160825
			25/26	Fig4D	20160825
Neuron Terra	3	Xp-Yp	24/25	Fig4D	20160527
			26/25	Fig4D	20160527
			26/25	Fig4D	20160323
	3	1q_2q_10q_1	15/16	Fig4D	20160323
			26/25	Fig4D	20160323
			17/18	Fig4D	20160527

	3	9p_15q_Xq_Y	17/18	Fig4D	20160527
			26/25	Fig4D	20160323
			L15/L16	Fig4D	20160624
	3	15q	26/25	Fig4D	20160323
			24/25	Fig4D	20160527
			26/25	Fig4D	20160527
	3	16p	L17/18	Fig4D	20160323
			17/18	Fig4D	20160527
			24/25	Fig4D	20160527
HIPS Subtel	3	TMEM132D E	24/25	Fig4A	20151028
			25/26	Fig4A	20151028
			25/26	Fig4A	20151028
		TMEM132C E	25/26	Fig4A	20161104
			25/26	Fig4A	20161104
			25/26	Fig4A	20161104
	4	RIMBP2	15/16	Fig4A	20160411
			17/18	Fig4A	20160411
			24/25	Fig4A	20160411
			25/26	Fig4A	20160411
	4	PTPRN2	17/18	Fig4A	20160411
			25/26	Fig4A	20160411
			17/18	Fig4A	20160420
			17/18	Fig4A	20160224
	4	AJAP1	17/18	Fig4A	20160420
			15/16	Fig4A	20160224
			17/18	Fig4A	20160224
			17/18	Fig4A	20160825
	3	STX2	15/16	Fig4A	20160224
			17/18	Fig4A	20160224
			15/16	Fig4A	20160311
	3	PRDM16	17/18	Fig4A	20160411
			15/16	Fig4A	20160224
			17/18	Fig4A	20160420
NPC Subtel	4	TMEM132D E	17/18	Fig4A	20151109
			15/16	Fig4A	20160429
			15/16	Fig4A	20150226
			17/18	Fig4A	20150226
	3	TMEM132C	17/18	Fig4A	20151109
			15/16	Fig4A	20161103
			17/18	Fig4A	20161103
	3	RIMBP2	17/18	Fig4A	20160429
			17/18	Fig4A	20160429
			17/18	Fig4A	20160429

	3	PTPRN2	17/18	Fig4A	20160429
			17/18	Fig4A	20160429
			17/18	Fig4A	20160429
	3	AJAP1	17/18	Fig4A	20160429
			17/18	Fig4A	20160429
			17/18	Fig4A	20160502
	4	STX2	17/18	Fig4A	20160429
			17/18	Fig4A	20160429
			17/18	Fig4A	20160429
			17/18	Fig4A	20160502
	4	PRDM16	17/18	Fig4A	20160429
			17/18	Fig4A	20160429
			17/18	Fig4A	20160429
			17/18	Fig4A	20160502
Neuron Subt	4	TMEM132D E	P15/16	Fig4A	20160323
			P16/17	Fig4A	20160323
			L15/16	Fig4A	20160323
			L17/18	Fig4A	20160323
	3	TMEM132C E	24/25	Fig4A	20160527
			17/18	Fig4A	20160527
			25/26	Fig4A	20160825
	4	RIMBP2	L17/L18	Fig4A	20160218
			P15/P16	Fig4A	20160218
			24/25	Fig4A	20160218
			25/26	Fig4A	20160218
	5	PTPRN2	24/25	Fig4A	20160527
			24/26	Fig4A	20160527
			24/25	Fig4A	20160527
			24/26	Fig4A	20160527
			17/18	Fig4A	20160527
	5	AJAP1	L15/L16	Fig4A	20160218
			P15/P16	Fig4A	20160218
			3mt P15/16	Fig4A	20160810
			3mt P17/18	Fig4A	20160810
			3mt 24/25	Fig4A	20160810
	4	STX2	L15/16	Fig4A	20160218
			L17/L18	Fig4A	20160218
			P15/P16	Fig4A	20160218
			P17/P18	Fig4A	20160218
	3	PRDM16	L17/L18	Fig4A	20160218
			P15/P16	Fig4A	20160218
			P17/P18	Fig4A	20160218

	N (biological	Telomereq	PC	Sample	Correspondir	Date of Experiments
HIPS	3	Telomere	15/16	Fig5A		20160503
			15/16	Fig5A		20160506
			15/16	Fig5A		20160328
NPC	4	Telomere	15/16	Fig5A		20160516
			17/18	Fig5A		20160516
			24/25	Fig5A		20160516
			17/18	Fig5A		20150421
Neuron	3	Telomere	15/16	Fig5A		20160405
			17/18	Fig5A		20160405
			17/18	Fig5A		20160415